Origin, ore forming fluid evolution and timing of the Logrosán Sn–(W) ore deposits (Central Iberian Zone, Spain)

Eva Chicharro [a,*], Marie-Christine Boiron [b], José Ángel López-García [a], Dan N. Barfod [c], Carlos Villaseca [d]

[a] Departamento de Cristalografía y Mineralogía, Facultad de Ciencias Geológicas, Universidad Complutense, 28040 Madrid, Spain
[b] GeoRessources, Université de Lorraine, UMR 7359, CNRS, Boulevard des Aiguillettes, BP 70239, F-54506 Vandœuvre-lès-Nancy, France
[c] NERC Argon Isotope Facility, Scottish Universities Environmental Research Centre, Rankine Avenue, Scottish Enterprise Technology Park, East Kilbride G75 0QF, UK
[d] Departamento de Petrología y Geoquímica, Facultad de Ciencias Geológicas, Instituto de Geociencias (UCM, CSIC), Universidad Complutense, 28040 Madrid, Spain

ABSTRACT

The Logrosán Sn–(W) ore deposits in the metallogenic Sn–W province of the European Variscan Belt consist of endo- and exogranitic greisen-type and quartz–cassiterite veins associated with a S-type granite. Mineral characterization, fluid inclusion study, isotope geochemistry and Ar–Ar geochronology have been combined in order to reconstruct the conditions for Sn–(W) mineralization. The endo- and exogranitic mineralization must have been developed in a relatively long-lived system (~308–303 Ma), during or soon after the emplacement of the Logrosán related-granite (at ca. 308 Ma). The mineralizing fluids are characterized by complex aqueous and volatile (H$_2$O–N$_2$–CO$_2$–CH$_4$–NaCl) fluid inclusions. Microthermometry and Raman analyses indicate that fluid composition evolved from N$_2$–CH$_4$ to N$_2$-rich, followed by CO$_2$-rich fluids, with varying amounts of H$_2$O. The presence of N$_2$ and CH$_4$ suggests the interaction with fluids derived from the nearby metasedimentary host rocks. A model of host-rock interaction, assimilation, and mixing of metamorphic and magmatic fluids, resulting in change of the redox conditions, is proposed for tin deposition. Later sulfide minerals were precipitated as a result of pressure and temperature release.

1. Introduction

The Sn–W metallogenic province of the European Variscan Belt contains numerous quartz–cassiterite and quartz–wolframite ores associated with highly evolved stanniferous Variscan S-type granites. They are granite-hosted or metasedimentary-hosted mineralization close to granite cupolas. Tin–tungsten styles of mineralization are mostly greisen, stockwork or vein types. Breccia pipes (Breiter et al., 1999), and sulfide replacement or skarn types (Cheilletz et al., 2005) are less often developed.

The relationship of Sn–W mineralization with magmatism is widely recognized (e.g., Lehmann, 1990; Burnham, 1997; Roedder, 1984; Pirajno, 1992). Differing interpretations of fluid inclusion and stable isotope data have led to competing hypotheses on the source of mineralizing fluids and the mechanisms of Sn–W concentration and precipitation. Magmatic, metamorphic, and meteoric waters have been proposed as sources of the metal-bearing fluids (e.g., Alderton and Harmon, 1991; Kelly and Rye, 1979; Wilkinson, 1990). Fluid mixing, interaction with the country rocks, and fluid immiscibility are some of the proposed mechanisms for ore deposition. An interval of several million years between the solidification of the related granite and the ore formation has been recorded for tin ore deposits (Lehmann, 1990). Geochronological data on tin–tungsten ore deposits in West and Central Europe have showed good agreement between the timing of granite emplacement and mineralization (Darbyshire and Shepherd, 1985; Snee et al., 1988; Chesley et al., 1993; Moura et al., 2014; Romer et al., 2007). Ar–Ar dating of muscovite combined with recent U–Pb direct dating on cassiterite show a coeval relationship of the ore with nearby cupolas of highly fractionated granites in Chinese deposits (Chen et al., 2014; Cheng et al., 2012; Cheng et al., 2013; Yuan et al., 2011; Zhang et al., 2014).

The aim of the present paper is to provide new geochemical, geochronological, fluid inclusion and isotopic data to better constrain the relationship and timing of the Logrosán granite and the associated Sn–(W) ore deposits. Geochemistry of fresh and altered (greisenized, muscovitized, sericitized) granites provide further constraints on the Sn–(W) mineralization. Mineral chemistry has been used for geothermometric estimates. Ar–Ar dating of muscovite allows determining the timing of mineralization. The ore fluid migration and deposition have been evaluated based on inferences from the application of combined microthermometry and Raman spectroscopy to complex fluid inclusion systems (H$_2$O–N$_2$–CH$_4$–CO$_2$–NaCl). In addition, isotopic studies allow us to infer the source of metal-rich fluids and the conditions of mineral precipitation. The integration of geochemistry, geochronology, isotopic and fluid inclusion data of the Logrosán ore deposits will contribute to the Sn–W deposit metallogenic model by: (1) better understanding the timing of ore fluid flow with regard to the emplacement and cooling

* Corresponding author.
E-mail addresses: evachicharro@ucm.es (E. Chicharro),
marie-christine.boiron@univ-lorraine.fr (M.-C. Boiron), jangel@geo.ucm.es
(J.Á. López-García), d.barfod@suerc.gla.ac.uk (D.N. Barfod), granito@ucm.es (C. Villaseca).
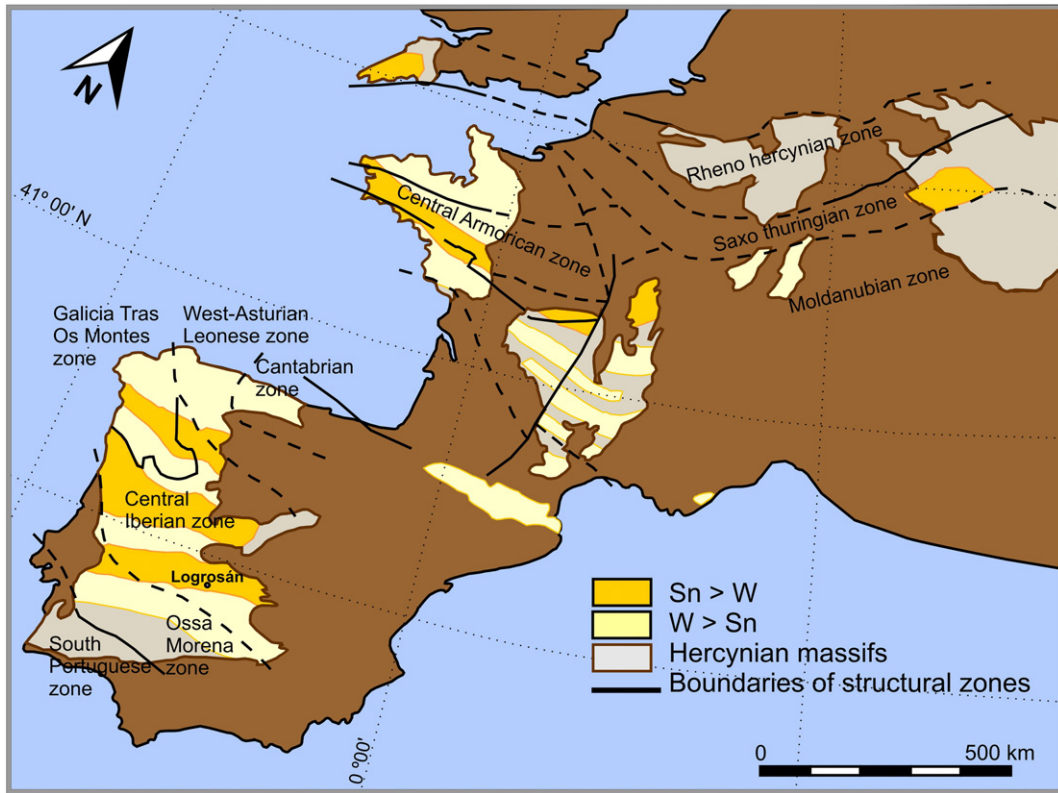
Fig. 1. Sn–W metallogenic province of the European Variscan Belt. Sn and W dominant bands.
Adapted from Derré (1982).

of the related granite bodies; (2) constraining the nature and sources of metal-rich fluids; and (3) determining the mineral precipitation conditions.

2. Geological setting

The Logrosán granite is located in the Central Iberian Zone (CIZ) of the Iberian Massif (southwestern Spain). This area corresponds to the

southwest extension of the Sn–W metallogenic province of the European Variscan Belt, formed as a consequence of the collision between Gondwana and Laurentia (Martínez Catalán et al., 1996; Villaseca et al., 2014; Romer and Kroner, 2015) (Fig. 1). The Variscan orogeny is characterized by extensive magmatism, that resulted in numerous granitic intrusions emplaced into a thick marine metasediment sequence, mostly Neoproterozoic in age, known in the southern CIZ as the Schist Greywacke Complex (SGC) (Fig. 2a) (e.g., Ribeiro, 1990;
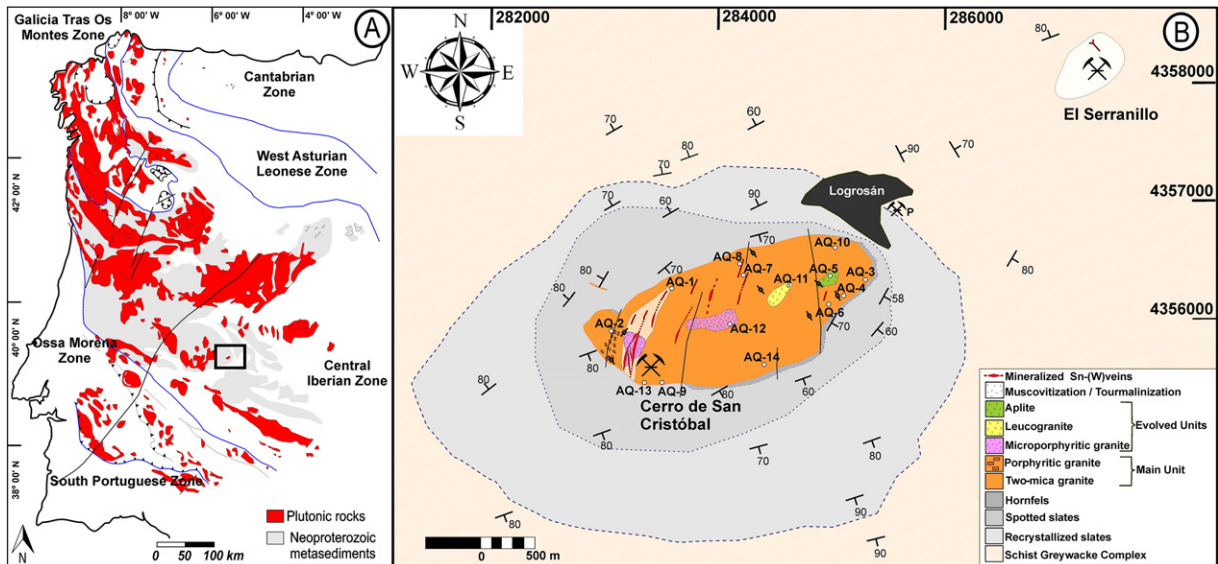

Fig. 2. (a) Schematic geological map of the Logrosán granite location in the Iberian Massif modified from Villaseca et al. (2014). (b) Detail of the Logrosán ore deposits (modified from Chicharro et al., 2015). Granite and greisen sampling points are indicated by open circles.

Table 1

Whole-rock major (wt.%) and trace-element (ppm) compositions of the Logrosán granite. Temperatures estimated using the saturation zircon temperature.[*]

Watson and Harrison (1983)

	Main Unit[*]						Evolved Units[*]			Altered granites			Greisen
	AQ1	AQ2	AQ4	AQ6	AQ13	AQ14	AQ5	AQ11	AQ12	AQ3	AQ9	AQ10	AQ7
SiO_2	72.46	72.26	72.53	73.93	73.12	74.03	72.94	72.73	74.01	70.49	66.79	63.59	49.75
Al_2O_3	14.43	14.76	15.24	15.14	14.92	14.94	15.30	14.42	14.83	16.58	17.67	19.38	31.61
FeO_t	1.25	1.71	1.33	0.82	1.37	1.14	0.78	1.45	1.17	1.38	2.18	1.00	1.83
MnO	0.02	0.02	0.02	0.02	0.02	0.02	0.01	0.02	0.02	0.03	0.03	0.01	0.04
MgO	0.28	0.33	0.38	0.16	0.33	0.24	0.22	0.22	0.26	0.35	0.48	0.23	0.75
CaO	0.59	0.45	0.69	0.50	0.54	0.51	0.46	0.25	0.46	0.31	0.30	0.40	0.07
Na_2O	3.68	2.67	3.31	3.87	3.31	3.42	3.27	2.95	2.95	2.30	3.04	4.28	1.37
K_2O	4.46	4.75	4.88	4.19	4.42	4.53	4.83	4.35	4.63	4.04	5.46	5.09	8.50
TiO_2	0.18	0.23	0.27	0.10	0.21	0.17	0.17	0.13	0.15	0.17	0.33	0.16	0.24
P_2O_5	0.50	0.47	0.57	0.57	0.49	0.46	0.54	0.51	0.55	0.42	0.63	0.78	0.04
LOI	1.33	2.55	1.62	1.51	1.47	1.08	1.95	1.98	1.74	3.29	2.90	4.09	5.86
Total	99.16	100.2	100.8	100.8	100.2	100.5	100.5	99.00	100.8	99.37	99.80	99.01	100.0
Sc	3.00	4.00	2.00	3.00	3.00	2.00	2.00	2.00	3.00	3.00	6.00	1.00	5.00
Be	15.00	23.00	16.00	11.00	14.00	18.00	7.00	19.00	9.00	7.00	12.00	10.00	15.00
V	7.00	12.00	10.00	<5	13.00	10.00	<5	10.00	9.00	8.00	21.00	7.00	15.00
Cr	<20	<20	<20	<20	<20	<20	<20	280	180.0	<20	<20	<20	<20
Co	2.00	4.00	3.00	3.00	2.00	2.00	2.00	2.00	2.00	2.00	2.00	1.00	1.00
Ni	<20	<20	<20	<20	<20	<20	<20	<20	<20	<20	<20	<20	<20
Cu	<10	20.00	<10	<10	20.00	<10	<10	<10	<10	<10	20.00	50.00	10.00
Zn	30.00	50.00	60.00	30.00	40.00	70.00	<30	70.00	<30	<30	100	60.00	100
Ga	21.00	23.00	25.00	20.00	22.00	21.00	20.00	24.00	20.00	34.00	34.00	26.00	91.00
Ge	2.20	2.10	1.70	2.30	2.30	2.10	1.50	3.40	2.50	2.70	2.90	2.20	3.80
As	60.00	51.00	137	94.00	137.0	64.00	123	44.00	103	1470	307	102	36.00
Rb	288	301	338	317	311	238	270	362	317	411	425	361	918
Sr	44.00	41.00	57.00	39.00	44.00	38.00	52.00	32.00	57.00	28.00	36.00	77.00	26.00
Y	6.90	5.20	7.60	5.50	7.60	9.60	5.40	3.30	6.60	7.00	6.00	7.40	13.10
Zr	76.00	80.00	118.00	43.00	82.00	77.00	74.00	60.00	62.00	79.00	101	94.00	42.00
Nb	8.70	11.70	10.10	13.60	11.40	9.00	9.60	15.90	11.10	11.60	21.30	10.40	21.00
Mo	<2	<2	<2	<2	<2	<2	<2	<2	<2	<2	<2	<2	<2
Ag	<0.5	0.50	<0.5	<0.5	<0.5	<0.5	0.70	<0.5	<0.5	1.00	<0.5	<0.5	<0.5

In	<0.1	0.10	<0.1	<0.1	<0.1	<0.1	<0.1	0.10	<0.1	0.20	0.10	<0.1	2.20
Sn	50.00	67.00	33.00	35.00	49.00	11.00	37.00	29.00	53.00	244	66.00	32.00	>1000
Sb	0.50	0.40	<0.2	0.70	<0.2	0.30	0.90	<0.2	0.50	0.90	<0.2	0.30	0.30
Cs	59.50	88.00	74.40	50.20	54.60	26.70	70.30	51.60	145.00	95.00	76.10	58.70	275.0
Ba	224	241	290	138.0	226.0	178.0	219.0	152	225	82.00	237	237	161.0
La	13.80	16.10	21.80	6.53	15.10	13.00	11.40	8.81	9.67	12.50	19.90	17.20	14.40
Ce	31.40	35.60	50.20	14.80	33.10	27.70	27.80	19.20	20.70	28.00	44.50	39.20	31.70
Pr	3.58	3.85	6.42	1.74	3.95	3.34	3.25	2.17	2.48	3.08	5.50	5.20	4.02
Nd	13.30	14.50	25.80	6.40	15.60	12.90	12.50	8.06	10.00	11.10	19.00	19.50	15.00
Sm	2.96	3.05	5.18	1.56	3.25	2.94	2.92	1.73	2.47	2.76	3.92	4.90	3.44
Eu	0.32	0.32	0.47	0.21	0.33	0.30	0.32	0.19	0.36	0.15	0.28	0.58	0.35
Gd	2.24	2.21	3.35	1.44	2.54	2.52	2.22	1.26	2.24	2.28	2.38	3.64	2.73
Tb	0.33	0.29	0.46	0.25	0.36	0.40	0.35	0.18	0.35	0.35	0.32	0.54	0.44
Dy	1.52	1.35	1.85	1.20	1.64	1.87	1.50	0.84	1.75	1.64	1.47	2.13	2.22
Ho	0.24	0.21	0.26	0.19	0.25	0.32	0.22	0.12	0.24	0.25	0.21	0.26	0.34
Er	0.60	0.52	0.60	0.51	0.66	0.86	0.46	0.30	0.51	0.64	0.50	0.59	0.84
Tm	0.09	0.07	0.08	0.07	0.09	0.12	0.06	0.05	0.06	0.10	0.07	0.08	0.10
Yb	0.56	0.49	0.44	0.53	0.52	0.71	0.37	0.30	0.38	0.66	0.42	0.45	0.57
Lu	0.08	0.07	0.06	0.07	0.08	0.11	0.05	0.05	0.06	0.09	0.07	0.06	0.08
Hf	2.20	2.40	3.00	1.50	2.60	2.50	2.50	1.70	2.10	2.50	3.10	3.10	1.20
Ta	2.26	3.08	2.50	4.76	3.73	1.97	1.98	4.00	2.30	3.27	5.70	2.06	3.07
W	24.60	82.10	74.20	36.00	23.90	9.00	131	1.60	376	155	27.90	29.40	51.50
Tl	1.84	1.98	2.02	1.99	1.87	1.40	1.77	1.56	1.79	2.25	2.87	2.43	4.69
Pb	28.00	22.00	29.00	21.00	24.00	28.00	26.00	21.00	29.00	10.00	31.00	40.00	8.00
Bi	0.30	<0.1	0.60	1.50	0.30	2.60	0.40	<0.1	0.60	3.30	7.70	0.50	0.70
Th	7.59	8.28	19.90	3.07	8.70	6.65	8.67	5.30	4.45	5.99	12.10	13.20	7.02
U	7.91	7.25	10.90	8.49	7.04	11.00	10.50	9.04	7.23	12.80	8.51	15.50	5.62
F		2003	1611	1150			1053			3063		1657	5495
Li		289.7	303.0	141.4			209.6			268.6		123.0	779.8
T (°C)[*]	738	755	777	699	752	746	744	734	733				

[*] Data from Chicharro et al. (2014).

Rodríguez Alonso et al., 2004). The Variscan orogeny in the CIZ is characterized by three deformation phases (D1, D2, and D3) and a later extensional fragile phase (D4) (Dias et al., 1998 and references therein). The Iberian granite emplacement is mostly syn-D3 (320–313 Ma), late-D3 (311–306 Ma), late-to-post-D3 (300 Ma), or even post-tectonic (299–290 Ma) (e.g., Dias et al., 2002). The massive granite emplacement at ca. 300–280 Ma generated heat flow anomalies that drove long-lived systems of significant hydrothermal activity throughout the upper crust (Mateus and Noronha, 2010). The Variscan shear zones that mostly developed during the D3 phase (coeval with the emplacement of some granites) were successively reactivated, forming a complex network of pathways that enabled fluid circulation. Some of the fluids may have carried significant amounts of metals in solution, such as Sn, W, Au, Cu and Pb (e.g., Mateus and Noronha, 2001, 2010). The numerous Iberian Sn–W ores are associated with the Variscan granites, forming the so-called Iberian Sn–W metallogenic province (Neiva, 1984).

The Logrosán pluton is a late-Variscan, S-type, tin-rich, phosphorous-rich, and peraluminous granite, emplaced at ca. 308 Ma into the Neoproterozoic SGC metasedimentary rocks (Chicharro et al., 2014). Its emplacement produced a zoned contact metamorphic aureole overprinting the greenschist-facies regional metamorphism (Chl-Bt). Two different units can be recognized in the Logrosán granite: the Main Unit and the Evolved Units (Chicharro et al., 2014). The Main Unit consists of a medium to coarse two-mica (muscovite > biotite) granite. The Evolved Units comprise aplitic, microporphyritic and altered granite sectors occupying the highest topographic areas of the pluton. The Logrosán ore deposits consist of greisen, veins, stockworks and disseminated mineralization in two settings: the endogranitic Cerro de San Cristóbal sector, and the exogranitic El Serranillo sector (Fig. 2b).

3. Materials and analytical methods

3.1. Whole-rock geochemistry

A total of 4 representative samples weighted between 3 and 5 kg were collected for whole-rock geochemistry (3 altered granites, and 1 greisen). These samples have been added to the Logrosán granite whole-rock dataset of Chicharro et al. (2014) (Table 1). Major analyses were carried out using fusion-inductively coupled plasma mass spectrometer (FUS-ICPMS) while trace elements were analyzed by fusion-inductively mass spectrometer (FUS-MS) at Activation Laboratories (Canada). Uncertainties in major elements range between 1 and 3% relative, except for MnO (5–10%). The precision for Rb, Sr, Zr, Y, V, Hf and most of the REE ranges from 1 to 5%, and between 5 and 10% for the other trace elements. Some granite samples show concentrations of certain elements below detection limits (V: 5 ppm, Cr: 20 ppm, Sc: 1 ppm, Co: 10 ppm). More information on the procedure, precision and accuracy of ACTLABS ICP-MS analyses can be found at www.actlabs.com. F and Li were determined in selected samples in the laboratory of the Spanish Geological and Mining Institute (IGME). Fluorine was determined by spectrophotometric methods after its extraction by pyrohydrolysis and Li was extracted by digestion with HF–HNO$_3$–HClO$_4$ and determined by atomic absorption spectrophotometry. An analytical error of ± 10% has been estimated.

3.2. Fluid inclusion study

Doubly-polished wafers (250–300 μm in thickness) for the fluid inclusion study from quartz–cassiterite and quartz–sulfide samples were analyzed using an Olympus BX-51 microscope-mounted Linkam THMSG600 heating-cooling stage at the Complutense University of Madrid. The calibration curve employed was generated from melting points of solid standards at T > 25 °C, and melting points of H$_2$O and H$_2$O–CO$_2$ of synthetic inclusions at T < 0 °C. The rate of heating was 0.1 °C/min when phase transitions were approached, in order to get

an accuracy of ± 0.2 °C for final ice melting at T < 0 °C, and of ± 4 °C for homogenization temperatures over 25 °C. The phase volume-fractions were visually estimated. Compositions of the volatile fluids were determined in individual inclusions by micro-Raman analyses performed on a Labram-type multichannel modular Raman spectrometer at GeoRessources laboratory (Université de Lorraine, Nancy, France).

3.3. Ar–Ar dating

Five samples from greisenized wall-rocks were selected for Ar–Ar dating. These samples were crushed, sieved, and washed in deionized water. High purity muscovite grains were handpicked under a binocular microscope, and cleaned using ethanol by ultrasonic treatment. Nuclear radiation was carried out on the Oregon State University reactor, Cd-shielded facility. Fish Canyon sanidine (28.294 ± 0.036 (1σ) Ma; Renne et al., 2011) was used to monitor ^{39}Ar production and establish neutron flux values (J) for the samples. Data were collected on a GVi instrument ARGUS 5-collector mass spectrometer at the SUERC (UK) using a variable sensitivity Faraday collector array in static collection (non-peak hopping) mode (Sparks et al., 2008; Mark et al., 2009). All data are blank, interference and mass discrimination corrected using the Massspec software package (authored by Al Deino, BGC). The plateau criteria are that the plateau consists of at least three contiguous steps and the scatter between the ages of the steps is low (MSWD close to 1), the fraction of ^{39}Ar released for these steps is ≥50%. Isochrons are calculated using only the plateau steps to confirm the composition of the trapped component. For plateau ages with MSWD > 1, we expand the age uncertainty (SEM) by a factor of (MSWD)$^{0.5}$ to account for "geological" scatter, i.e., non-analytical sources of uncertainty.

3.4. Stable isotopes

Stable isotope data were obtained at the Stable Isotope Laboratories of the Salamanca University. Whole rock samples and mineral separates of unaltered granite, greisen, veins, and country host rocks were analyzed for oxygen and hydrogen isotope composition. Quartz, muscovite, tourmaline, and cassiterite were separated by handpicking after crushing to 80–120 mesh. ^{18}O/^{16}O determinations were carried out by laser fluorination using a conventional vacuum extraction line (Clayton and Mayeda, 1963), but employing ClF$_3$ as reagent (Borthwick and Harmon, 1982). The evolved oxygen gas was converted to CO$_2$ on a red hot carbon rod. The ^{18}O/^{16}O ratios were determined on the CO$_2$. H$_2$ and H$_2$O extraction for D/H isotopic analyses were carried out by the uranium technique described by Godfrey (1962), with modifications introduced by Jenkin (1988), heating the samples at temperatures up to 1500 °C. The water was converted to hydrogen gas by reduction over hot depleted uranium. The hydrogen and oxygen isotope ratios were measured in a SIRA-II mass spectrometer and data are reported in the normal denotation relative to V-SMOW.

Sulfur isotopes were determined for two endogranitic polished blocks and one exogranitic polished block. Sulfide samples were analyzed by in situ combustion using a Nd:YAG laser (12 W, l = 1.060 n) connected to a mass spectrometer and microinlet system (VG SIRA-II). The polished blocks were inserted into a sample chamber which was evacuated, and subsequently filled with an excess of oxygen gas (Fallick et al., 1992; Kelley and Fallick, 1990). Laser calibration data for arsenopyrite and chalcopyrite were taken from the study of Wagner et al. (2004) and Kelley and Fallick (1990). A series of in situ laser combustions is either made of single 100 to 200 μm diameter spots or thin (~50 μm) long channels, so as to avoid heterogeneities. The SO$_2$ gas produced was subsequently cryogenically purified in order to eliminate the O$_2$ and CO$_2$ gases, and then analyzed on a VG SIRA II gas mass spectrometer. The precision and accuracy of the isotopic measurements ranged from + 0.2‰ to + 0.9‰ (1σ).

4. Results

4.1. Paragenetic sequence and mineralogy

Based on petrological and microscopic observations, a general para-
genetic diagram for the Logrosán ore deposits has been established
(Fig. 3). Three stages are recognized: (1) Oxide Stage, (2) Sulfide
Stage, and (3) Supergene Stage.

(1) The Oxide Stage (Stage I) is the main ore stage. It is characterized
by columbite, Nb–Ta rutile, and cassiterite precipitation. The
Oxide Stage is divided in two sub-groups. The host-rock alter-
ation sub-group is mostly composed of greisenized granite mar-
ginal to quartz–cassiterite veins (Fig. 4a), and is characterized by
disseminated Nb–Ta phase mineralization, cassiterite, minor
wolframite, and sulfides, such as molybdenite and minor arseno-
pyrite (Apy Ia). The vein sub-group (Fig. 4b) is characterized by
the main cassiterite precipitation, with Nb–Ta phase inclusions,
minor wolframite and euhedral arsenopyrite (Apy Ib). Tourma-
line also occurs as a late phase.
(2) The Sulfide Stage (Stage II) consists of the sulfide suite precipita-
tion; arsenopyrite and stannite are the dominant minerals
(Fig. 4c). Most arsenopyrite (Apy II) precipitated early during
the paragenetic sequence, and usually presents euhedral to
subeuhedral habits. Löllingite has been recognized in the cores
of Apy II. Arsenopyrite forms intergrowths and curvilinear equi-
librium grain boundaries with stannite. Arsenopyrite II also

contains rounded crystals of stannite, sphalerite, chalcopyrite
and minor pyrrhotite, suggesting co-precipitation of these
phases (Fig. 4d). The presence of stannite, sphalerite, and chalco-
pyrite as replacement patches and along fractures in Apy II indi-
cates that they formed continually at different times during the
Sulfide Stage. Moreover, sphalerite single crystals include minute
blebs of chalcopyrite. Stannite also occurs as small blebs of
exsolution-type in sphalerite, and vice versa. Galena and Ag–Pb
sulfosalts may occur as inclusions together with sphalerite in
stannite. Minor native bismuth and bismuthinite intergrowths
are found as inclusions within arsenopyrite and within sphalerite
enclosed in Apy II. Bismuthinite and native bismuth intergrowths
are also found as isolated crystals. Other minor sulfides, such as
molybdenite, tetrahedrite, digenite and bornite have been
found locally. Calcite and siderite are present as a very late phase.
(3) The Supergene Stage (Stage III) is characterized by the presence
of natanite (an iron–tin hydroxide mineral) replacing cassiterite.
Hematite and goethite may occur along fractures as secondary
weathering products in these oxidizing zones. Secondary sulfides
such as chalcocite and covellite replaced primary sulfides.

4.2. Granite geochemistry

Altered granites and greisen show significant geochemical differ-
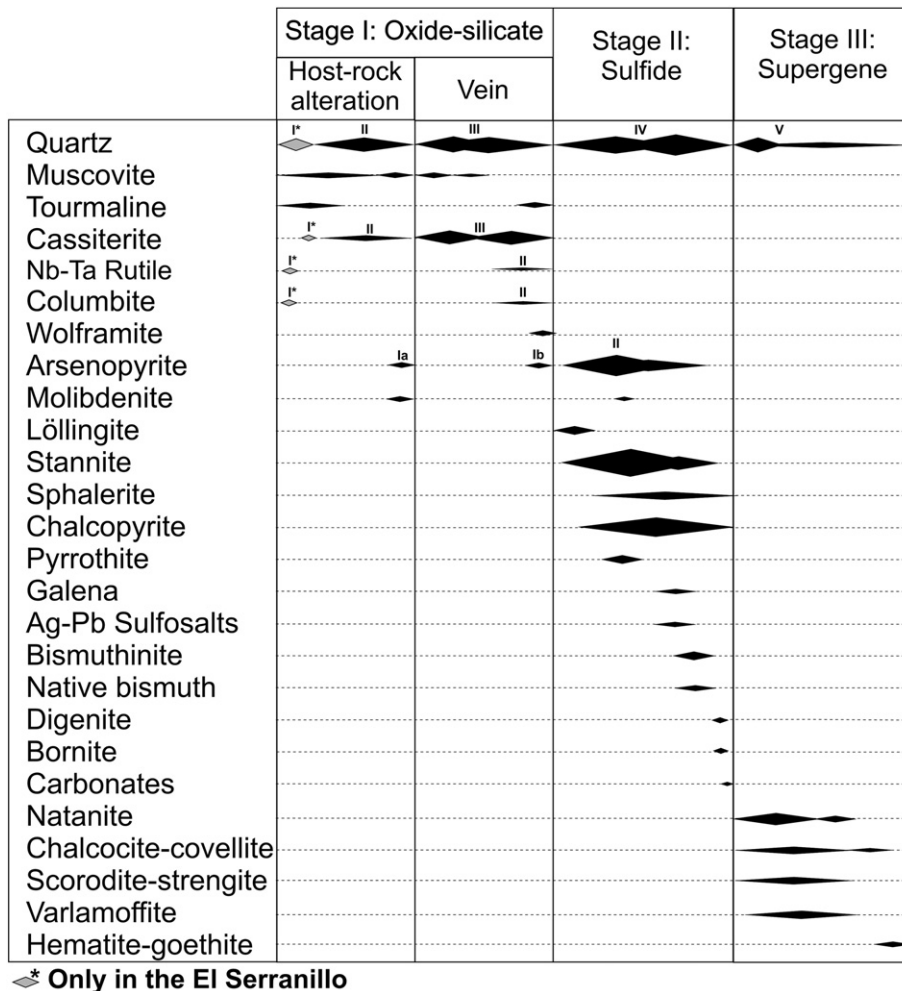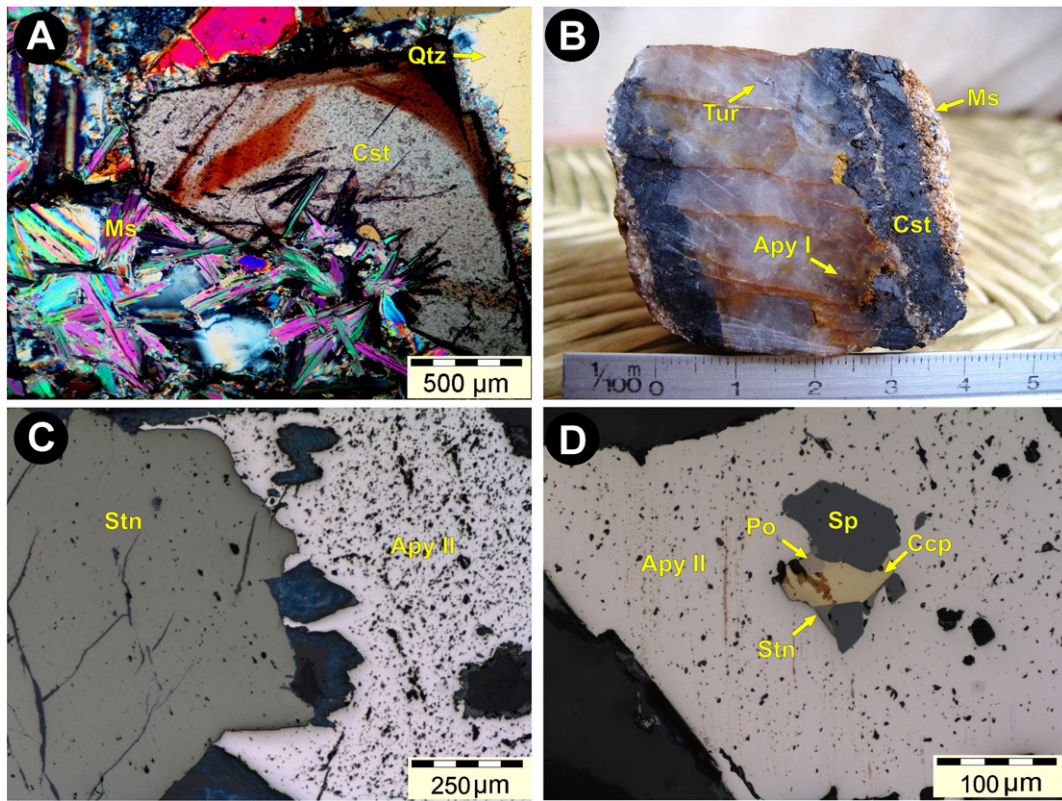ences with regard to the Main and Evolved Units (Table 1) (Figs. 2b

Fig. 3. Paragenetic sequence scheme for the Logrosán ore deposits, modified from Chicharro et al. (2015).

Fig. 4. (a) Photomicrograph in transmitted light (x nicols) of greisen-type alteration with strongly zoned cassiterite (Cst), muscovite (Ms) and quartz (Qtz). (b) Photograph of a hand specimen of a typical quartz–cassiterite veinlet, with a muscovite (Ms) selvage and late tourmaline (Tur) needles. (c) Photomicrograph in reflected light (parallel nicols) of an arsenopyrite (Apy II) and stannite (Stn) intergrowth. (d) Photomicrograph in reflected light (parallel nicols) of an arsenopyrite (Apy II) crystal containing inclusions of stannite (Stn), sphalerite (Sph), chalcopyrite (Cpy) and minor pyrrhotite (Po).
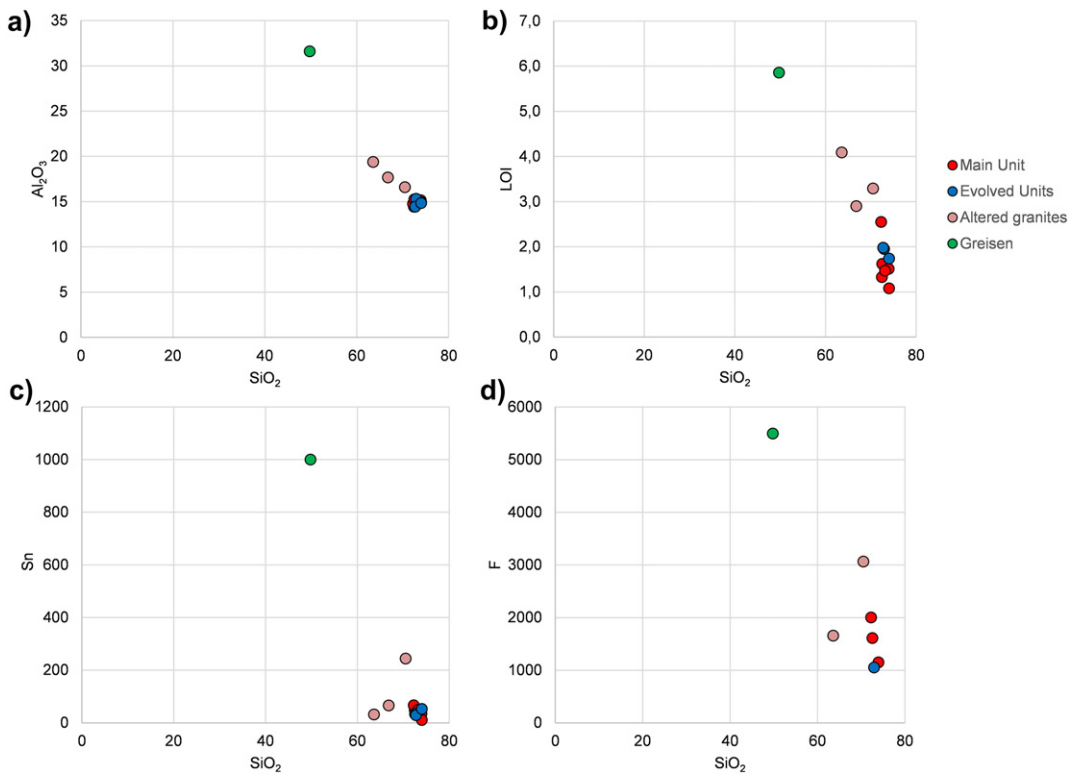
Fig. 5. Selected major (wt.%) and trace (ppm) element variation diagrams versus SiO_2 for the Logrosán granite.

and 5). They are depleted in SiO_2 and highly enriched in Al_2O_3, due to muscovitization, sericitization and chloritization (Fig. 5a). Altered granites and greisen are Rb-enriched, which can be explained by the substitution of K during the hydrolysis of feldspars. They have higher loss on ignition values (LOI: 2.90–5.86%) (Fig. 5b), suggesting elevated volatile contents (i.e., boron and fluorine). High F contents in samples correspond to the higher Sn contents (Fig. 5c and d). Sn even reaches values above the upper limit of detection in the greisen (in Table 1 see AQ7: Sn > 1000 ppm).

4.3. Mineral geochemistry

Cassiterite from the Logrosán greisen and veins is a very pure SnO_2 phase, with trace substitution of Fe, Ti, Nb, and Ta. Zoned cassiterite shows Fe, Nb, and Ti enrichment and Sn depletion in darker zones. Nb–Ta rutile is heterogenous, with Nb > Ta and variable Ti and Nb contents. Columbite from Logrosán corresponds to the iron-rich member of the columbite group and has variable Nb, Ta, and Ti contents. Detailed descriptions of cassiterite and Nb–Ta phases are given in Chicharro et al. (2015).

Representative sulfide compositions from the Logrosán veins are listed in Table 2. Arsenopyrite is a ubiquitous sulfide mineral in the Stage I and Stage II. A total of 99 analyses have been performed on arsenopyrite from greisen, quartz–cassiterite and quartz–sulfide samples. Arsenopyrite from the Oxide Stage (Apy I) is characterized by small (~200 μm), isolated euhedral crystals. The proportion of Fe ranges from 34.06 to 34.69 at.%. The proportion of As (32.70–34.41 at.%) varies inversely with S (31.03–32.80 at.%). In the Sulfide Stage, arsenopyrite (Apy II) develops euhedral to subeuhedral grains, up to few mm across, co-precipitating first with löllingite, and subsequently with pyrrhotite, sphalerite, stannite and chalcopyrite. Individual crystals are mostly homogeneous, though some show zoning with variations higher than

Table 2
Average composition of sulfide minerals from the Logrosán ore deposits (Apy: arsenopyrite, Stn: stannite; Sp: sphalerite, Ccp: chalcopyrite, Po: pyrrhotite).

Mineral	Apy I	Apy II	Stn	Sp	Ccp	Po
Stage	Oxide	Sulfide	Sulfide	Sulfide	Sulfide	Sulfide
N	19	80	59	30	20	3
Zn wt.%	0.01	0.04	3.58	60.73	1.48	0.23
Ag	–	0.01	0.16	0.55	0.06	b.d.l.
Co	–	0.04	0.16	0.02	0.03	0.07
Bi	–	0.07	0.10	0.07	0.12	0.14
Ni	–	0.01	0.00	0.01	0.02	b.d.l.
Fe	35.34	34.92	8.91	3.85	29.11	58.32
Mn	–	b.d.l.	0.02	0.04	0.05	b.d.l.
Cu	0.01	0.10	28.91	0.67	34.60	0.12
Cd	–	0.02	0.09	0.84	0.02	0.03
Sn	b.d.l.	0.02	27.92	0.33	1.29	b.d.l.
Sb	–	0.06	b.d.l.	0.07	0.04	0.05
Pb	0.10	0.10	0.19	0.14	0.16	0.22
As	45.83	45.97	b.d.l.	0.02	0.03	0.03
S	18.95	18.66	29.26	33.32	33.70	39.79
Total	100.24	100.02	99.30	100.65	100.70	98.99
Zn at.%	0.01	0.04	3.00	44.96	1.05	0.15
Ag	–	0.00	0.07	0.25	0.03	0.00
Co	–	0.04	0.04	0.01	0.03	0.05
Bi	–	0.02	0.02	0.02	0.03	0.03
Ni	–	0.01	0.00	0.00	0.01	0.00
Fe	34.46	34.25	8.76	3.34	24.19	45.51
Mn	–	0.00	0.00	0.04	0.04	0.00
Cu	0.01	0.08	24.99	0.51	25.27	0.08
Cd	–	0.01	0.03	0.36	0.01	0.01
Sn	0.00	0.01	12.93	0.14	0.50	0.00
Sb	–	0.03	0.00	0.03	0.01	0.02
Pb	0.03	0.03	0.05	0.03	0.04	0.05
As	33.31	33.61	0.00	0.01	0.02	0.01
S	32.19	31.88	50.11	50.31	48.79	54.09

1 at.% As from core to rim. The Fe content ranges from 32.91 to 35.19 at.%. The As and the S contents are inversely proportional. Sulfur varies from 30.13 to 33.79 at.%, while As shows a wide range of variation from 31.62 to 35.11 at.%.

4.4. Ar–Ar thermochronology data

Ar–Ar analyses for five muscovite samples from altered host-rocks and selvages related to cassiterite mineralization were performed (Table 3). The samples produced relatively undisturbed spectra and well-defined plateaux. The plateau ages vary from 303 ± 3 to 311 ± 3 Ma, with MSWD values from 0.86 to 2.47, representing reliable crystallization ages for the muscovite from the altered host-rocks and vein samples. The isochron ages are consistent with these results, giving ages from 290 ± 20 to 308 ± 3 Ma.

4.5. Fluid inclusion study

Fluid inclusions suitable for microthermomety and Raman analyses have been found in quartz and cassiterite from quartz–cassiterite and quartz–sulfide veins. More than 250 microthermometric and 85 Raman measurements have been performed on four samples of quartz–cassiterite and quartz–sulfide veins from the Logrosán ore deposits.

4.5.1. Fluid inclusion petrography

Fluid inclusions are widespread in the quartz–cassiterite and quartz–sulfide vein samples. They occur mostly in quartz, but also in cassiterite. Samples from three distinct mineralized veins have been studied, occurring in the Stage I (Oxide Stage) and/or Stage II (Sulfide Stage).

Type-I fluid inclusions occur only in Stage I. They occur exclusively in cassiterite and are distributed along growth zones, indicating a primary origin, following the Roedder (1984) criteria. Visual estimations of the volumetric fraction of vapor phase range from 30 to 40 vol%. They are rather dark in appearance, ranging from 5 to 40 μm in size. They feature irregular, elongated, and oblate shapes. Larger fluid inclusions are isolated, while smaller ones appear as trails, following crystal growth orientations (Fig. 6a).

Type-II fluid inclusions are widespread in samples from Stage I and Stage II. Their sizes range generally from 20 to 50 μm. The volumetric fractions of vapor phase show wide variations from 30 to 80 vol%. They occur as isolated fluid inclusions in quartz–sulfide samples, suggesting a primary origin in these samples. They also occur in clusters and isolated fluid inclusions randomly distributed within quartz in quartz–cassiterite samples (Fig. 6b). Type-II fluid inclusions may punctually occur within cassiterite, but they do not follow any crystallographic direction. More often, Type-II fluid inclusions are found within quartz adjacent to cassiterite and sulfide grains.

Type-III fluid inclusions appear mainly in Stage II. They are usually found along healed fractures, occurring locally together with Type-II fluid inclusions (Fig. 6c). They range in size from 5 to 50 μm, with a high vapor phase fraction (FV from 97 to 100 vol%). They show rounded, subrounded, elongated, and irregular shapes, as well as negative crystal shapes.

Type-IV fluid inclusions are found predominantly in Stage II. Their sizes vary between 10 and 40 μm and they appear as negative crystals. The volumetric vapor fraction estimated visually is 100 vol%. They are confined mainly to vuggy parts of the quartz–sulfide veins, suggesting a late origin (Fig. 6d). They may appear locally as intragranular trails in quartz from quartz–cassiterite veins.

Type-V aqueous fluid inclusions are secondary and occur in all studied samples. Type-V aqueous fluid inclusions are found as transgranular trails. Their sizes vary between less than 5 μm and 50 μm, smaller fluid inclusions tend to have elongated shapes, while larger ones are rather irregular. The vapor phase estimated is below 20%.

Table 3
Summary of ^{40}Ar/^{39}Ar data of muscovite from the Logrosán ore deposits.

Sample	Location	Plateau age (Ma) ±2σ	MSWD	Steps	%^{39}Ar	Isochron ages (Ma) ±2σ	^{40}Ar/^{36}Ar$_{(i)}$ ±2σ	MSWD	Integrated age (Ma) ±2σ
L104	San Cristóbal (endogranitic)	308 ± 3	1.43	12	98.1	304 ± 4	400 ± 90	1.2	307 ± 4
L105		311 ± 3	2.47	6	72.7	302 ± 7	450 ± 110	0.027	303 ± 4
L107		306 ± 2	1.16	5	62.4	308 ± 10	250 ± 190	1.5	303 ± 3
L111		308 ± 3	0.86	15	64.9	290 ± 20	800 ± 900	0.48	298 ± 3
SER	El Serranillo (exogranitic)	303 ± 3	1.53	6	69.9	301 ± 9	350 ± 190	1.8	297 ± 3

4.5.2. Microthermometry and Raman spectroscopy: results and interpretation

Microthermometric and Raman data, bulk compositions, salinity, and densities of the Logrosán fluid inclusions are summarized in Table 4.

Phase transitions were observed between −180 and +30 °C by microthermometry. Van den Kerkhof (1988, 1990) and Van den Kerkhof and Thiéry (2001) proposed a division of carbonic fluid inclusions in H-type and S-type. This classification is based on phase transitions of carbonic phases upon freezing and then, warming runs. H-type fluid inclusions have homogenization as the final phase transition (Th > Tm) while in S-type fluid inclusions, sublimation or melting is the final phase transition (Th < Tm). We have followed this classification for the volatile phase of Logrosán fluid inclusions, owing to the N_2 and CH_4 high contents identified by Raman spectroscopy on the volatile phase.

Molar volumes have been estimated on the basis of binary N_2–CH_4 model (Van den Kerkhof, 1988, 1990; Thiéry et al., 1994) or CO_2–N_2 model (Thiéry et al., 1994). Bulk composition calculations have been done after the Ramboz et al. (1985) method. The salinity calculations (expressed as wt.% NaCl equiv.) using the Bodnar (1993) equation are a rough estimate, owing to the lack of experimental studies for complex N_2–CO_2–CH_4–H_2O–NaCl compositional fluid inclusion systems. Isochores were calculated with the program ISOC (Bakker, 2003) using the EOS of Duan et al. (1992, 1996) for Type-I and Type-II fluid inclusions; using the EOS of Flowers (1979) and Holloway (1977) for Type-III and Type-IV fluid inclusions; and the H_2O–NaCl fluid inclusions were calculated from the EOS of Knight and Bodnar (1989).

4.5.2.1. Type-I: mixed N_2–CH_4 aqueous–volatile inclusions.
These inclusions consist of N_2–CH_4-bearing aqueous–volatile inclusions. The volatile phase is referred to as the H1 subtype (Th$_{N_2–CH_4}$) inclusions proposed by Van den Kerkhof (1988); i.e., L + V → L. Accurate microthermometric observations in these fluid inclusions are difficult because of their dark appearance and the high birefringence of the host cassiterite. N_2–CH_4 homogenization (Th$_{N_2–CH_4}$) was observed only for a few specimens. Homogenization of the volatile phases occurs to the liquid between −135.1 and −127.2 °C. Ice melting temperatures (Tm$_{ice}$), when observable, range between −3.6 and −0.2 °C. Melting clathrate temperatures (Tm$_{cl}$) yield values between 4.9 and 9.6 °C. Total homogenization (Th) occurs to the liquid, and less frequently to the vapor, from 336.9 to 397.6 °C. Raman analyses of the volatile phase shows N_2 contents between 44 and 74 mol%, and CH_4 contents between 26 and 56 mol%. The bulk composition of Type-I fluid inclusions shows 93.8–96.8 mol% H_2O, 1.4–4.1 mol% N_2, and 1.1–2.8 mol% CH_4. The bulk density of Type-I fluid inclusions ranges from 0.64 to 0.73 g/cm^3. Salinity ranges from 0.35 to 6 wt.% NaCl equiv.
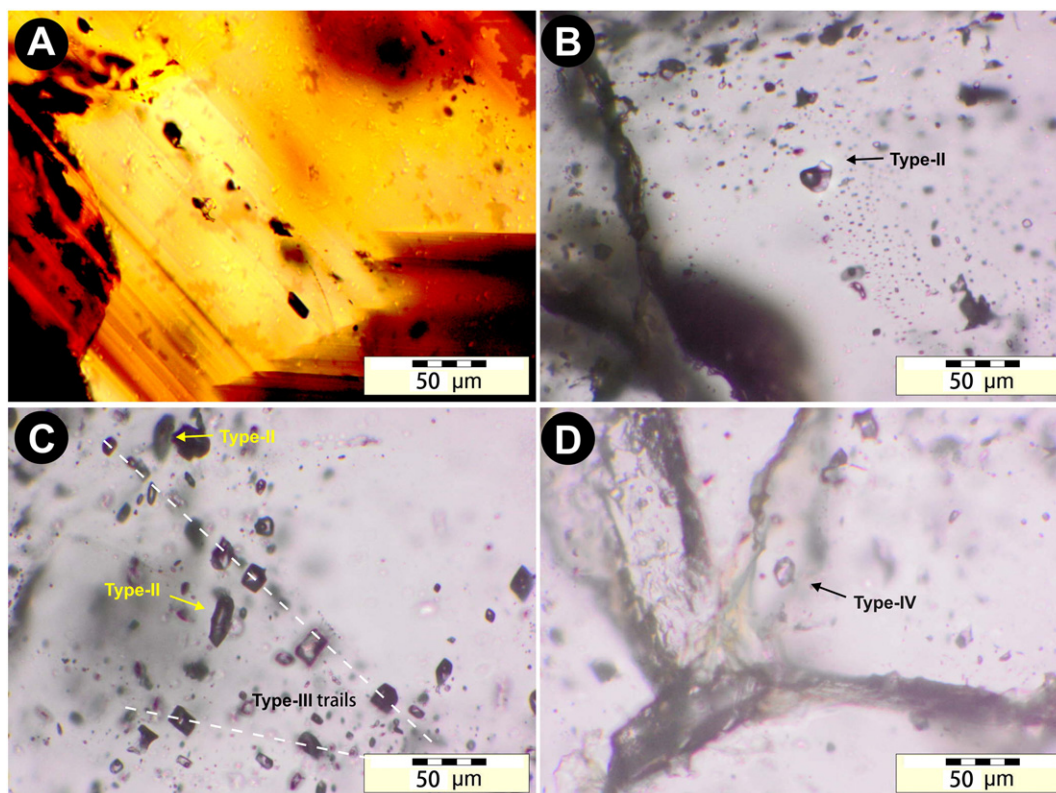
Fig. 6. (a) Type-I primary fluid inclusions oriented along a crystal growth band in cassiterite. (b) Type-II primary isolated fluid inclusion. (c) Type-III secondary trails cutting Type-II primary FIA's. (d) Type-IV primary fluid inclusions in late quartz.

Table 4
Summary of microthermometric (°C) and Raman data of fluid inclusions from the Logrosán ore deposits.

	Type I	Type II	Type III	Type IV	Type V
Phase stage	Stage I	Stage I/Stage II	Stage II	Stage II	Stage III
Mineral host	Cassiterite	Quartz	Quartz	Quartz	Quartz
Composition	N_2–CH_4	N_2–CO_2–CH_4	N_2-rich	CO_2-rich	H_2O
FV (%)	30/40	30/80	97/100	100	<20
Microthermometry (°C)					
$Th_{N_2-CH_4}$	−135.1/−127.2	−135.5/−101.7	−133.2/−124.8	−128.4/−92.2	–
Tm_{CO_2}	–	−86.8/−57.2	−68.5/−62.3	−62.1/−60.0	–
Tm_{cl}	4.9/9.6	4.1/15.2	11.2/12.2	–	–
Tm_{ice}	−3.6/−0.2	−7.4/−0.2	–	–	−2.7/−1.2
Th_{CO_2}	–	−34.2/7.5	–	−40.2/−8.2	–
Th	336.9/397.6	280.0/389.8	–	–	152.2/258.5
Raman (mol.%)					
ZN_2	43.9/74.1	16.8/67.0	51.5/67.1		–
ZCO_2	–	13.7/65.3	18.9/33.2		–
ZCH_4	25.9/56.1	7.00/34.3	13.5/16.3		–
Bulk composition (mol.%)					
XH_2O	93.8/96.8	53.3/98.4	0.00/39.6	–	97.2/98.7
XN_2	1.4/4.1	0.3/27.4	36.8/57.7	15.9/37.5	–
XCO_2	–	0.9/15.6	13.1/31.4	52.3/79.7	–
XCH_4	1.1/2.8	0.3/12.5	8.3/16.3	4.5/10.1	–
Carbonic phase type	H1	S2/(H4)	S2	H4	–
NaCl (% equiv.)	2.1/4.5	0.4/11.0	–	–	2.1/4.5
Global density (g/cm³)	0.64/0.73	0.26/0.74	0.07/0.10	0.04/0.13	0.83/1.02

4.5.2.2. Type-II: mixed H_2O–N_2–CO_2–CH_4 aqueous–volatile inclusions.
Type-II volatile phase corresponds to the S2 subtype ($Th_{N_2-CH_4} \rightarrow Tm_{CO_2}$) proposed by Van den Kerkhof (1988), i.e., thus showing $S + L + V \rightarrow S + L(V) \rightarrow L(V)$. The microthermometric data measured on warming yield partial homogenization to liquid ($Th_{N_2-CH_4}$) between −135.5 and −101.7 °C and melting or sublimation of solid CO_2 (Tm_{CO_2}) at −86.8 to −57.2. Clathrate melting temperatures (Tm_{cl}) range from 4.1 to 15.2 °C. Ice melting temperatures (Tm_{ice}) were measured between −0.2 and −7.4, corresponding to salinities between 0.3 and 11 wt.% NaCl equiv., with an average value of 4.8 wt.% NaCl equiv. A few number of fluid inclusions included in Type-II show homogenization of CO_2 (Th_{CO_2}), observed to vapor phase in a large range of temperatures from −40.2 to 7.2 °C. Their volatile phase should be classified as H4 ($Th_{N_2-CH_4} \rightarrow Tm_{CO_2} \rightarrow Th_{CO_2}$; i.e., $S + L + V \rightarrow S + L \rightarrow S + L + V \rightarrow L + V \rightarrow V$). The total homogenization (Th) of Type-II fluid inclusions was either to liquid or vapor and frequently the inclusions decrepitated. The total homogenization temperatures vary between 320.9 and 389.8 °C, although some fluid inclusions decrepitated from 280 °C. Bulk composition is: 53.3–98.4 mol% H_2O, 0.3–27.4 mol% N_2, 0.8–15.6 mol% CO_2, and 0.3–12.5 mol% CH_4. Traces of H_2S have been recognized by Raman spectrometry. The bulk density ranges from 0.26 to 0.74 g/cm³. Two groups can be distinguished, high-density and low-density Type II, regarding the L/V ratio. The heterogeneity in the Type-II fluid inclusion suggests a possible immiscibility.

4.5.2.3. Type-III: N_2-rich vapor fluid inclusions. The N_2 > CO_2–CH_4 fluid inclusions correspond to the S2 group defined by Van den Kerkhof (1988) ($Th_{N_2-CH_4} \rightarrow Tm_{CO_2}$); i.e $S + L + V \rightarrow S + L \rightarrow L$. During cooling, the volatile phase heterogenizes at about −100 °C and homogenizes ($Th_{N_2-CH_4}$) between −133.2 and −124.8 °C to liquid. Melting of CO_2 (Tm_{CO_2}) has been recorded between −68.5 and −62.3 °C. Clathrate temperatures could be measured for two fluid inclusions, yielding temperatures of 11.2 and 12.2 °C. Type-III volatile fluid inclusions have a very low density (0.07–0.11 g/cm³). Bulk composition shows H_2O contents between 0 and 53.7 mol%; the volatile phases are characterized by high N_2 contents (28.8–57.7 mol%), and moderate CO_2 (8.9–31.4 mol%) and CH_4 (6.47–16.3 mol%) contents.

4.5.2.4. Type-IV: CO_2-rich vapor fluid inclusions. The CO_2 > N_2–CH_4 gas-rich fluid inclusions can be characterized as H4 ($Th_{N_2-CH_4} \rightarrow Tm_{CO_2} \rightarrow Th_{CO_2}$) after the Van den Kerkhof (1988) classification; i.e., $S + L + V \rightarrow S + L \rightarrow S + L + V \rightarrow L + V \rightarrow V$. Homogenization to liquid ($Th_{N_2-CH_4}$) yields temperatures from −128.4 to −92.2 °C, this is not always identified. CO_2 melting temperatures (Tm_{CO_2}) are in the range of −63.2 to −60.0 °C. The homogenization of CO_2 (Th_{CO_2}) was observed to vapor in a varied range of temperatures from −40.2 to 8.2 °C. Their bulk density is very low (0.04–0.13 g/cm³). The bulk composition is free of water and shows high CO_2 contents (52.3–79.7 mol%). N_2 ranges from 15.9 to 37.5 mol% and CH_4 varies between 4.47 and 10.1 mol%.

4.5.2.5. Type-V: secondary aqueous fluid inclusions. The secondary water-rich H_2O ± (N_2–CH_4–CO_2) inclusions show water volume contents >80%. Melting of ice (Tm_{ice}) is observed at temperatures from −1.2 to −2.7 °C (2.1 to 4.5 wt.% NaCl equiv.). Traces of N_2, CH_4 and CO_2 have been recorded by Raman spectroscopy. Total homogenization temperatures (Th) were achieved between 152 and 258 °C, showing a frequency maximum at 230 °C, and a minor maximum at 160 °C (Fig. 7).

4.6. Stable isotope data: geothermometry and isotope signature of the fluids

4.6.1. Oxygen and hydrogen isotopes
The $\delta^{18}O$ and δD values of whole rock, quartz, muscovite, cassiterite and tourmaline from SGC metasedimentary rocks, granite, pegmatite, early quartz–tourmaline veins, greisen, and quartz–cassiterite veins are presented in Table 5. Temperature ranges for the isotope composition of fluids have been estimated by a combination of isotope geothermometry (see Section 4.6.2. (Isotope geothermometry)), paragenetic criteria, and fluid inclusion homogenization temperatures.

Whole rock SGC metasediments have $\delta^{18}O_{SMOW}$ values of 13.1 and 13.4‰, and δD_{SMOW} values of −67.3 and −52.6‰. These values are typical for low- to medium-grade metamorphosed sedimentary rocks (Sheppard, 1986; Hoefs, 2009). Whole rock granite samples studied correspond to one Main Unit sample ($\delta^{18}O_{SMOW}$ of 14.1‰, and δD_{SMOW} of −84.7‰), and two Evolved Unit samples. The Evolved Units display higher $\delta^{18}O_{SMOW}$ (14.5 and 15.0‰) and δD_{SMOW} values (−77.9 and −77.0‰).

Muscovite from the granite and quartz from pegmatites (magmatic stage) show similar $\delta^{18}O_{fluid}$ values (muscovite: 13.7–14.3‰; quartz: 13.4–14.1‰). Tourmaline from pegmatites has lower $\delta^{18}O_{fluid}$ (13.0 to 13.3‰) than magmatic muscovite and quartz, since it is a later phase.
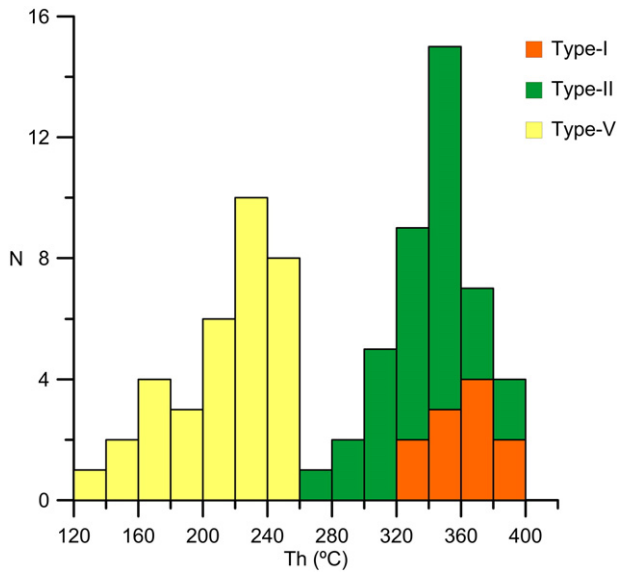
Fig. 7. Histograms of homogenization temperature for Type-I, Type-II and Type-V fluid inclusions.

Similarly, δD_{fluid} of magmatic muscovite ranges from -75.5 and $-71.4‰$, while δD_{fluid} of tourmaline varies from -67.3 to $-72.6‰$.

Quartz and tourmaline from quartz–tourmaline veins (metasomatic stage) show $\delta^{18}O_{fluid}$ values of 12.8–13.5‰, and 13.3–13.4‰, respectively; δD_{fluid} of metasomatic tourmaline ranges between -61.6 and $-66.9‰$.

Minerals from altered host rocks and quartz–cassiterite veins (hydrothermal stage) show values of $\delta^{18}O_{fluid}$ in a relatively large range varying from 10.00 to 14.6‰ (quartz: 10.0–14.2‰; cassiterite: 12.3–12.4‰; muscovite: 12.8–14.6‰; and tourmaline: 10.9–12.7‰). Muscovite and tourmaline δD_{fluid} estimates show relatively high variabilities (muscovite: -53.4 to $-80.1‰$; tourmaline: -60.7 to $-70.1‰$).

4.6.2. Isotope geothermometry

Isotope geothermometers have been used to constrain the temperature of the magmatic, metasomatic, and hydrothermal stages in the Logrosán ore deposits (Table 6).

A quartz–tourmaline pair from a pegmatite (magmatic stage) yields a temperature of 716 °C. This temperature is consistent with the calculated Logrosán granite saturation zircon temperatures (Table 1).

Tourmaline from quartz–tourmaline veins (metasomatic stage) yields temperatures between 793 and 836 °C. This implies an important release of boron following the granite emplacement.

The quartz–cassiterite and quartz–muscovite pairs provide information about the temperatures during the mineralization event (hydrothermal stage). The quartz–muscovite isotope thermometry provides a large range of temperatures, from 410 to 688 °C. The Cerro de San Cristóbal vein samples (L104 and L105) show more reliable temperatures (410 and 542 °C). On the contrary, the exogranitic El Serranillo samples (SER-1) show higher temperatures (606 and 688 °C). These high temperatures are most likely attributed to disequilibrium between the quartz and the analyzed muscovite. Temperatures calculated from coexisting quartz and cassiterite (hydrothermal stage) show a relatively small range between 457 and 536 °C (an average value of 514 °C). This is in agreement with the temperature obtained for tourmaline of quartz–cassiterite veins (450 ± 60 °C). A temperature between 450 and 530 °C has been established as the best fit for the cassiterite precipitation. This range of temperature is in reasonable agreement with primary fluid inclusion homogenization temperatures recorded in cassiterite (<400 °C) (Table 4), and with the arsenopyrite geothermometry (see Section 4.6.4. (Arsenopyrite geothermometry)).

4.6.3. Sulfur isotopes

The sulfur isotope data are presented in Table 7 as conventional per mil values ($\delta^{34}S‰$) referenced to the Canyon Diable Troilite (CDT) standard, and calculated for the laser corrected factor. $\delta^{34}S_{CDT}$ values of arsenopyrite (from -2.5 to $-5.5‰$) and chalcopyrite (from -2.4 to $-3.7‰$) are in the same range. The $\delta^{34}S_{H_2S}$ composition of the fluid has been calculated for given temperatures determined on the basis of

Table 5
O/D stable isotope data of granite, metasediments and associated hydrothermal alteration and mineralization from Logrosán.

Mineral	Rock type	Sample	Parag. stage	$\delta^{18}O$ (‰ SMOW)	δD (‰ SMOW)	%H$_2$O	Tmin	Tmax	$\delta^{18}O$ fluid min	$\delta^{18}O$ fluid max	δ^1D fluid min	δD fluid max
Whole rock	Metasediments	CEG-1		13.1	−52.6	3.8	–	–	–	–	–	–
		CEG-2		13.2	−67.3	1.7	–	–	–	–	–	–
		CEG-2		13.4	−67.3	1.7	–	–	–	–	–	–
	Granite	AQ2	N	14.1	−84.7	1.4	–	–	–	–	–	–
		AQ-5	E	14.5	−77.9	1.3	–	–	–	–	–	–
		AQ-12	E	15.0	−77.0	1.2	–	–	–	–	–	–
Quartz	Pegmatite[5]	L-179		14.3	–	–	700	800	14.1	13.4	–	–
	Qtz-Tur vein[5]	L-108		13.7	–	–	700	800	13.5	12.8	–	–
	Altered host-rocks[1]	SER-5	Qtz I	14.1	–	–	450	540	11.0	12.4	–	–
		SER-1	Qtz II	15.8	–	–	450	540	12.7	14.1	–	–
		L-104	Qtz II	16.5	–	–	450	540	13.4	14.8	–	–
	Qtz-Cst vein[1]	L-105	Qtz II	15.8	–	–	450	540	12.7	14.1	–	–
		L-111	Qtz III	15.1	–	–	450	540	12.0	13.4	–	–
Muscovite	Granite[6],[7]	AQ1		12.9	−75.6	4.4	700	800	14.3	13.7	−71.4	−75.5
	Altered host-rocks[2],[7]	SER-1	Ms I	14.0	−76.6	3.5	450	540	13.3	14.3	−53.4	−62.3
		SER-1	Ms I	14.3	−76.6	3.5	450	540	13.6	14.6	−53.4	−62.3
		L-104	Ms I	13.5	−94.4	4.4	450	540	12.8	13.8	−71.2	−80.1
	Qtz-Cst vein[2],[7]	L-105	Ms II	13.7	−81.8	4.1	450	540	13.0	14.0	−58.6	−67.5
Cassiterite	Altered host-rocks[3]	L-104	Cst II	8.2	–	–	450	540	12.4	12.4	–	–
	Qtz-Cst vein[3]	L-111	Cst III	8.1	–	–	450	540	12.3	12.3	–	–
		L-111	Cst III	8.2	–	–	450	540	12.4	12.4	–	–
		L-165	Cst III	8.2	–	–	450	540	12.4	12.4	–	–
Tourmaline	Pegmatite[4],[8]	L-179		12.7	−94.5	3.3	700	800	13.3	13.4	−67.3	−72.6
	Qtz-Tur vein[4],[8]	L-108		12.4	−88.8	3.2	700	800	13.3	13.1	−61.6	−66.9
		L-108		12.3	−88.8	3.2	700	800	13.3	13.0	−61.6	−66.9
	Qtz-Cst vein[4],[9]	L-65.2	Tour II	13.2	−92.6	3.3	350	450	10.9	12.7	−60.7	−70.1

Oxygen composition of fluids ($\delta^{18}O_{fluid}$): [1]Clayton et al. (1972), [2]O'Neil and Taylor (1967), [3]Zheng (1991), [4]Zheng (1993), [5]O'Neil (1986) and [6]Bottinga and Javoy (1975) and hydrogen composition of fluids (δD_{fluid}): [7]Suzuoki and Epstein (1976), [8]Guo and Qian (1997) and [9]Jiang (1998).

Table 6
Stable isotope geothermometry of the Sn–(W) deposits from the Logrosán area.

Sample		Mineral pair	$\delta^{18}O_{Qtz}$	$\delta^{18}O_{mineral}$	Temperature (°C)[a]
Chacko et al. (1996)					
SER1	Altered host-rocks	Qtz–Ms	15.8	14.0	606 ± 52
SER1		Qtz–Ms	15.8	14.3	688 ± 70
L104		Qtz–Ms	16.5	13.5	410 ± 24
L105	Qtz–Cst vein	Qtz–Ms	15.8	13.7	542 ± 41
Polyakov et al. (2005)					
SER1	Altered host-rocks	Qtz–Cst	15.8	8.2[b]	530 ± 11
L104		Qtz–Cst	16.5	8.2	457 ± 10
L104		Qtz–Cst	15.8[b]	8.2	494 ± 11
L111	Qtz–Cst vein	Qtz–Cst	15.1	8.1	530 ± 12
L111		Qtz–Cst	15.1	8.2	536 ± 13
L165		Qtz–Cst	15.1[b]	8.2	536 ± 13
Zheng (1993)					
L179	Pegmatite	Qtz–Tur	14.3	12.7	716 ± 77
L108	Qtz–Tur vein	Qtz–Tur	13.7	12.4	836 ± 100
L108		Qtz–Tur	13.7	12.3	793 ± 91
Kotzer et al. (1993)					
65.2	Qtz–Cst vein	Qtz–Tur	15.1[b]	13.2	541 ± 60

[a] Assuming an error of 0.1‰ for $\delta O_{mineral}$.
[b] Isotopic value of an equivalent sample.

fluid inclusion studies, chemical geothermometry and paragenetic criteria for chalcopyrite. The $\delta^{34}S$ composition of the fluid for arsenopyrite cannot be calculated, as no fractionation factor exists for this mineral phase. The $\delta^{34}S_{H_2S}$ composition of chalcopyrite samples varies between −2.3 and −3.6‰.

4.6.4. Arsenopyrite geothermometry

The dependence of arsenopyrite composition on equilibration conditions, such as temperature and sulfur activity, has been used as a geothermometer for temperatures higher than 300 °C by Kretschmar and Scott (1976), and reexamined by Sharp et al. (1985). Iron arsenides, or other iron sulfides, have not been recognized accompanied the arsenopyrite (Apy I) in the Oxide Stage, this makes the application of the arsenopyrite geothermometer not possible. However, arsenopyrite from the Sulfide Stage (Apy II) has been identified enclosing relict patches of löllingite and pyrrhotite. Zoned arsenopyrite crystals with compositional variations in As higher than 1 at.% have not been considered. Accordingly, 42 analyses of unzoned arsenopyrite crystals were selected. To determine the ore forming conditions, we assumed the equilibration of arsenopyrite, first with löllingite, and later, with pyrrhotite. The average compositions of arsenopyrite from different samples and the calculated temperatures are summarized in Table 8. Temperatures obtained (456–417 °C) represent the highest temperatures of the Sulfide Stage. Moreover, the geothermometer of Nekrasov et al. (1979) has been applied to sphalerite–stannite pairs in samples where sphalerite and stannite are closely intergrown. A range of temperatures between 453 and 372 °C for the following steps of the Sulfide Stage is estimated.

Table 7
Sulfur isotope data of the Logrosán ore deposits.

Sample	Location	Mineral	$\delta^{34}S_{CDT}$ (‰)	Laser correction factor (‰)	T (°C)	$\delta^{34}S_{H_2S}$ (‰)
-4.2	Endogranitic	Apy	−5.9	−5.5	430	–
L-4.2	Endogranitic	Apy	−5.3	−4.9	430	–
L-5.1	Endogranitic	Apy	−2.9	−2.5	430	–
L-5.1	Endogranitic	Apy	−3.9	−3.5	430	–
SER-4	Exogranitic	Cpy	−3.1	−2.4	370	−2.3
SER-4	Exogranitic	Cpy	−4.5	−3.8	370	−3.6
SER-4	Exogranitic	Cpy	−3.5	−2.8	370	−2.7

Table 8
Average of As (at.%) content and estimated temperature ranges for arsenopyrite geothermometry of arsenopyrite (Apy) from the Logrosán ore deposits.

| Sample	at.% As				Estimated temperature (°C)
	Average	SD	Range	N	
L-4.2	34.08	0.35	33.42–34.74	11	456 ± 10
L-13	33.90	0.54	33.03–34.82	12	442 ± 10
L-4.3	33.73	0.58	32.67–34.45	7	438 ± 10
L-5	33.35	0.88	32.09–34.04	4	416 ± 20
L-5.3	33.34	0.60	32.69–34.16	5	415 ± 10
L-12	33.37	0.60	32.70–33.86	3	417 ± 10

5. Discussion

5.1. Timing of the Logrosán ore deposits

The Logrosán granite yields an U–Pb ID-TIMS age of 307.88 ± 0.86 (2σ) Ma and a weighted average $^{206}Pb/^{238}U$ age of 303.0 ± 2.3 (2σ) Ma (Chicharro et al., 2014). In this work, we obtained muscovite Ar–Ar ages from 303 to 311 Ma, with 2σ errors of ±2–3 Ma (Table 3). Muscovite of endogranitic samples (San Cristóbal) yield Ar–Ar ages of 306–311 Ma, in part anomalously older than the granite emplacement. The exogranitic sample (SER) is slightly younger than the endogranitic samples (303 ± 3 Ma), although overlapping with analytical error. The El Serranillo ore deposit is directly related to the Logrosán granite, which extends towards this area in depth, as revealed by gravity survey (Chicharro et al., 2015). Moreover, there are strong similarities on the paragenetic, textural and geochemical features of endogranitic and exogranitic occurrences. Therefore, we infer that the exo- and endogranite mineralization resulted from the same hydrothermal activity. The slight difference in timing between endogranitic and exogranitic mineralization suggests that there were at least two different hydrothermal pulses.

The narrow range of ages from 308 to 306 Ma is considered to be the timing of the main endogranitic Sn–(W) mineralization; a second hydrothermal pulse related to the exogranitic mineralization may have occurred soon after (306–303 Ma). These ages overlap the emplacement timing of the genetically related granite (308 ± 0.8 Ma) and are quite consistent, assuming that the longevity of the associated hydrothermal system is expected to be at around 2 Ma (e.g., Kent and McDougall, 1995; Sillitoe, 1994). Similar timing has been recognized for the Variscan Sn–W ore deposit related to the Carris granite (Portugal) by Moura et al. (2014). Sn–W contemporaneous to the granite-related emplacement has been also recorded, for instance, for the tin mineralization in the Dadoushan deposit of the Gejiu district (China) (Cheng et al., 2012), or the Xuebaoding Sn–W–Be deposit (China) (Zhang et al., 2014).

5.2. Nature and origin of mineralizing fluids

The isotopic compositions of fluids at equilibrium with the magmatic (granite and pegmatite), metasomatic (quartz–tourmaline veins) and hydrothermal (altered host-rocks and quartz–cassiterite veins) minerals are represented in Fig. 8. The $\delta^{18}O_{fluid}$ values decrease and the δD_{fluid} values increase from the magmatic to the hydrothermal minerals (Fig. 8). We may expect a rise of δO_{fluid} and a drop of δD_{fluid} values for decreasing temperatures if the system remained closed, according to the mineral isotopic equilibration equations. The inverse evolution reflects the equilibration with ^{18}O-depleted and D-enriched fluids in an open system.

In the conventional $\delta^{18}O$–δD diagram (Fig. 9) the standard fields for different types of water (Sheppard, 1986; Ohmoto, 1986) are shown and compared with the calculated fluid signatures for tourmaline and muscovite from granite, pegmatite, quartz–tourmaline, altered host-rocks, and quartz–cassiterite samples. The fields of the isotopic composition of the Logrosán granite and SGC metasediments are outlined. The
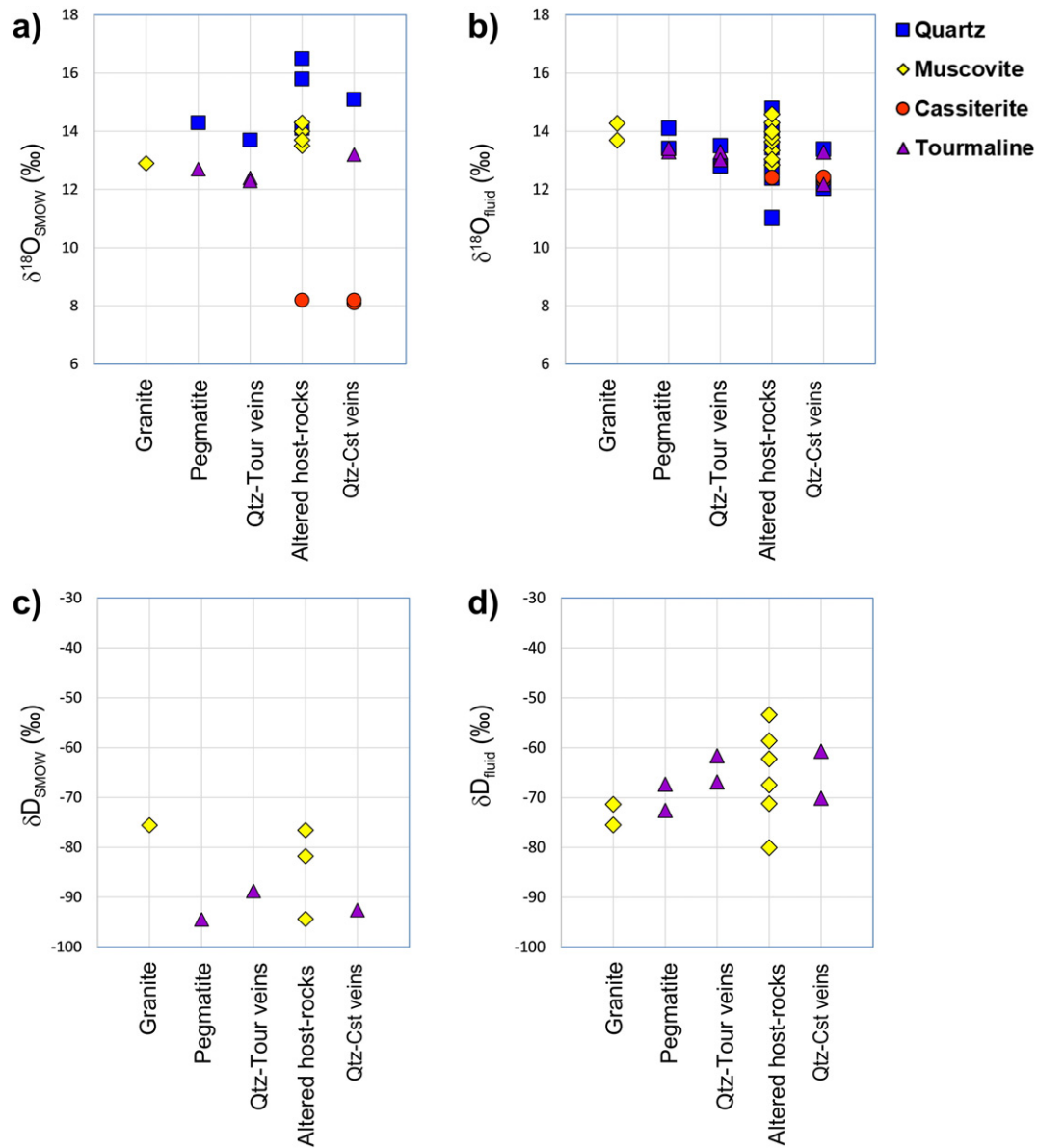
Fig. 8. Plot of mineral isotopic signature vs. time represented by granite, pegmatite, quart–tourmaline veins, host-rock alteration and quartz cassiterite vein for: (a) $\delta^{18}O_{mineral}$; (b) $\delta^{18}O_{fluid}$; (c) $\delta D_{mineral}$; (d) δD_{fluid}.
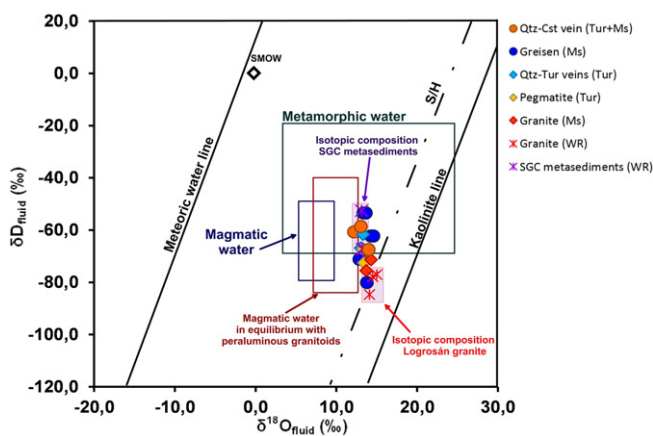
Fig. 9. δO–δD plot of the isotopic compositions of fluids from Logrosán. SMOW: Standard Mean Ocean Water.
Reference data: Sheppard (1986); Ohmoto (1986) and Craig (1961).

granite whole-rock samples display a rising trend through the supergene/hypogene line, which is probably related to the hydrothermal kaolinization process (Sheppard et al., 1969). The Logrosán granite whole rock isotopic analyses show higher $\delta^{18}O$ values than the field of the peraluminous Cornubian granites outlined by Sheppard (1977). $\delta^{18}O$ values higher than 10‰ have been found in Variscan granites from Western Europe (Tartèse and Boulvais, 2010; Hoefs and Emmermann, 1983) and the southern CIZ (e.g., Castelo Branco Batholith, Antunes et al., 2008). These elevated $\delta^{18}O$ values are typical of high-SiO$_2$ peraluminous granites, notably for those derived from a sedimentary or metasedimentary protolith (Taylor, 1978). The SGC metasedimentary isotopic field overlaps with the metamorphic field defined by Taylor (1974). The minerals vary isotopically in a vertical path, towards higher δD values (Fig. 9). The δD signature of minerals and rocks are very sensitive to the δD composition of interacting fluids because hydrogen is a minor component of most minerals and rocks (Rollinson, 1993). Muscovite and tourmaline of the magmatic stage (granite and pegmatite) plot close to the magmatic water in equilibrium with the peraluminous granitoid field and below the metamorphic water field. Tourmaline of the metasomatic stage plots in the

metamorphic water field. Muscovite, tourmaline and cassiterite of the hydrothermal stage (quartz–cassiterite veins and greisen) mostly plot in the metamorphic field. Mixing with a metamorphic-derived fluid of higher δD and lower δO composition may explain the trend observed from magmatic to hydrothermal minerals.

The Logrosán ores show negative $\delta^{34}S$ values corresponding to a light source of sulfur (Table 7). Data of $\delta^{34}S$ vary between -5.5 and $-2.4‰$. There is very little variation in the $\delta^{34}S$ values of arsenopyrite from endogranitic ore deposits and chalcopyrite from exogranitic ore deposits, although arsenopyrite reaches the highest values. This is consistent with the fact that chalcopyrite forms generally at lower temperatures, while arsenopyrite forms in a wider temperature range during the whole Sulfide Stage. These relatively uniform and narrow $\delta^{34}S$ composition suggests a homogeneous source for the endo- and exogranitic ore deposits (Ohmoto and Rye, 1979). The $\delta^{34}S$ signature of S-type granites is expected to be the same as the $\delta^{34}S$ signature of the sulfur minerals, since the H_2S fractionation between sulfur minerals and granitic melts is negligible (Ohmoto, 1986). Sulfur minerals from magmatic sources have $\delta^{34}S$ signatures between -5 and 5‰ (Ohmoto and Rye, 1979) and below 0‰ for ilmenite-series granitoids formed by partial melting of predominantly sedimentary protoliths (Ishihara and Sasaki, 1989). Little variations in the $\delta^{34}S$ signature of individual arsenopyrite crystals, showing values below $-5‰$, are supposed to respond to a decrease of $\delta^{34}S$ at the beginning of the Sulfide Stage. This would explain the precipitation of sulfide minerals by an increase of the fO_2 as a consequence of a new fluid input (Ohmoto, 1972). More oxidized conditions may be the combination of this oxidized fluid input and boiling (Dubessy et al., 1987), which is also inferred from the fluid inclusion data.

5.3. Fluid evolution

The fluid inclusion studies in the Logrosán ore deposits show complex compositions (N_2–CO_2–CH_4–H_2O) (Fig. 11), which have been recognized in other granite-related ore deposits (e.g., Dewaele et al., 2015; Dolníček et al., 2012; Fu et al., 2014; Giuliani, 1984; Liao et al., 2014; Moura et al., 2014; Noronha et al., 1999; Vindel et al., 1996; Ortega et al., 1996; Pohl and Günther, 1991; Wilkinson, 1990). The volatile composition evolution and the estimated isochores for the different fluid inclusion types are presented in Figs. 10 and 11, respectively. The primary low-salinity N_2–CH_4–H_2O Type-I fluid inclusions have significant proportions of N_2 and CH_4 (Fig. 10). The N_2 more likely derives from the hydrolysis of feldspars during the regional metamorphism, while the CH_4 probably derives from organic matter sources (e.g.,

Cepedal et al., 2013; Huff and Nabelek, 2007; Dubessy et al., 1989; Shepherd et al., 1991; Roedder, 1984). The SGC metasediments are thought to be the primary source of nitrogen and methane. The lack of carbonic material in inclusions suggests that CH_4 was assimilated during fluid migration by the reaction between poorly organized carbonic material and magmatic fluids (Xu, 2000). Assimilation of CH_4–N_2 from metasedimentary host rocks by fluids related to Sn–W mineralization in granites has been pointed out previously by Wilkinson (1990) and Pohl and Günther (1991). The cassiterite precipitated due to the interaction of metamorphic-derived fluids with probable magmatic fluids in an open system. This is in agreement with the altered host rocks and quartz–cassiterite vein oxygen and hydrogen isotopic compositions. The presence of pure magmatic fluids are not known, but are inferred by the introduction of CO_2 in Type-II fluid inclusions and by the stable isotope constraints. The lack of CO_2 in the oldest preserved fluid (Type-I) may be attributed to the carbon volatilization and/or leaching during contact metamorphism (Linnen and Williams-Jones, 1995). Another possibility is that CO_2 was not introduced in the system, but generated by the oxidation of CH_4 (Fuertes-Fuente et al., 2000). However, the wide range of compositional volatile-phase proportions in successive fluids (Type-II, Type III and Type-IV fluid inclusions) rather suggest that CO_2 was mainly introduced by the magmatic derived-fluid. The mixing between two fluids of different sources, magmatic and metamorphic, produced this immiscibility. Fluid mixing for ore precipitation have been described for similar Sn–W ore deposits (e.g., Giuliani, 1984; Giuliani et al., 1988; Pohl and Günther, 1991; Noronha et al., 1999; Wilkinson, 1990; Martínez-Abad et al., 2015). Fluids related to Type-II fluid inclusions are associated with the Sulfide Stage. Type-II fluid inclusions are very heterogeneous, with different vapor–water ratios and compositions (Table 4, Fig. 10). The CO_2 in these fluid inclusions indicates a higher O_2 fugacity (Eugster and Wilson, 1985), which is in agreement with $\delta^{34}S$ isotopes. The high-density and low-density Type-II fluid inclusion isochores intersect at approximately 400 °C and 100 MPa (Fig. 11). Intersecting isochores may indicate the P–T trapping conditions for the heterogeneous mixture of N_2–CO_2–CH_4 and water (Roedder and Bodnar, 1980). The heterogeneity of Type-II fluid inclusions preserved in quartz accompanying the sulfides suggests that their formation is related to effervescence (phase separation). This process was due to a decrease in pressure and temperature as a result of hydraulic fracturing. We suggest that subsequent Type-III and Type-IV fluid inclusions (both recognized as secondary in early quartz) are the consequence of immiscibility. Intermittent effervescence may have resulted in the separation of N_2–CH_4 from CO_2 for Type-III and Type-IV fluid inclusions (Fig. 10a). This would explain the lower water contents
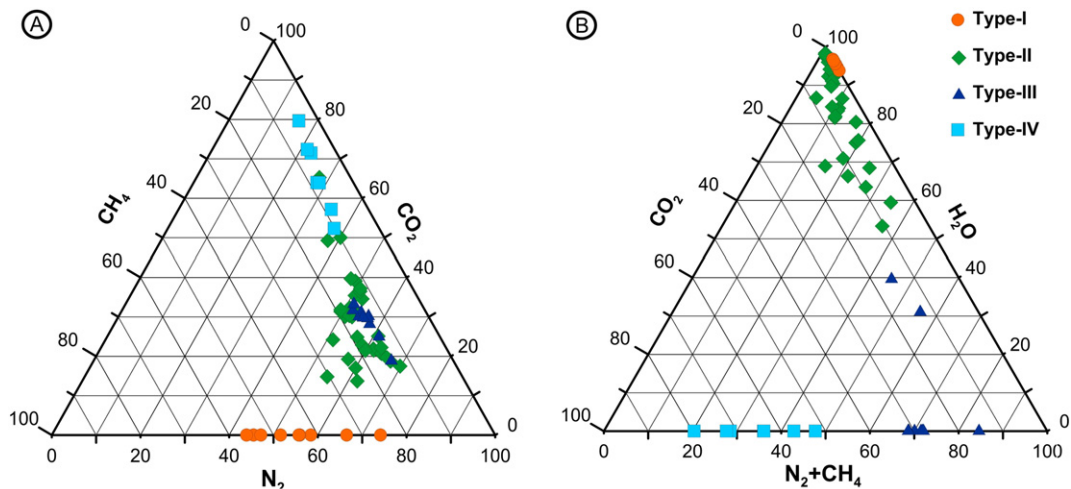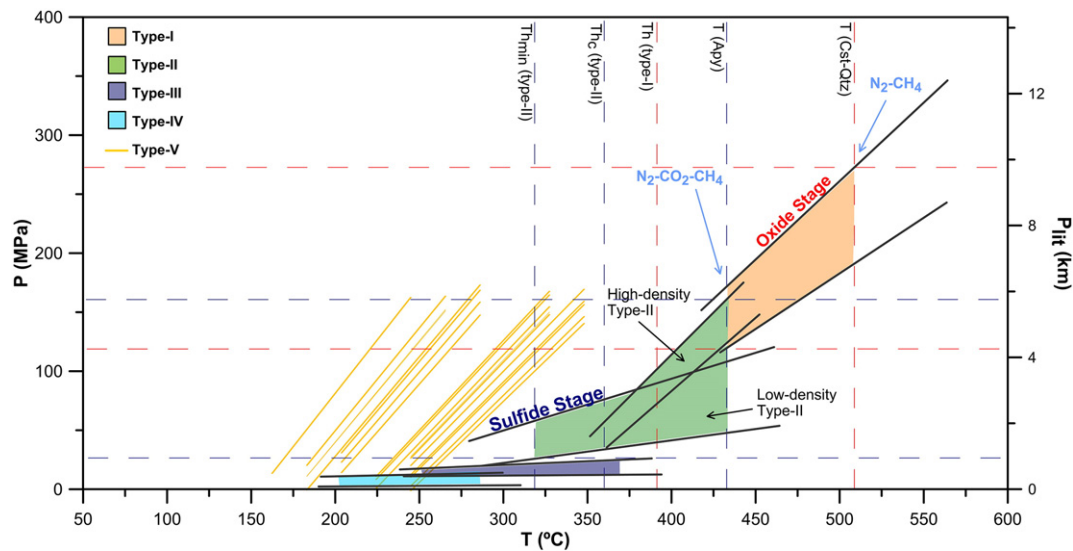

Fig. 10. (a) XN_2–XCO_2–XCH_4 and (b) $X(N_2 + CH_4)$–XH_2O–XCO_2 ternary diagrams showing the carbonic and bulk composition of the Logrosán ore deposits fluid inclusions.

Fig. 11. Pressure–temperature reconstruction of conditions prevailing in the Logrosán ore deposits; data from geothermometry, critical homogenization (Thc) and homogenization temperatures (Th) of fluid inclusions.

in fluid inclusions with time (Fig. 10b). The last episodes recognized in the system are represented by aqueous Type-V fluid inclusions and correspond to the influx of cool meteoric fluids.

5.4. Controls of Sn–(W) mineralization

The cassiterite mineralization is almost contemporaneous with the Logrosán granite emplacement. The source of tin is assumed to be magmatic, as Sn is being enriched during the fractionation of the Logrosán granite (Table 1). The relatively high F contents in the Logrosán granite, especially in the altered units (Table 1, Fig. 5), suggest that tin may have been transported as a Sn(II)–fluoride complex (Yushan and Shuqing, 1986). Tin must have been transported under reduced conditions (Burnham and Ohmoto, 1980; Ishihara, 1977). Some authors have attributed greisenization as the major and probably sole control on cassiterite precipitation in greisen-hosted tin deposits (Halter and Williams-Jones, 1996). The host-rock greisen-like alteration in the Logrosán ore deposits consists mainly of narrow vein muscovite-rich selvages and alteration patches. Neutralizing reactions (hydrolysis of feldspars) by increasing the surface contact area between the hydrothermal fluids and the aluminosilicate rocks are more effective in structural weakness zones (e.g., the stockworks from the El Serranillo sector) (Chicharro et al., 2015). The alteration found in the Logrosán ore deposits may have contributed to the ore precipitation, but it is unlikely to be the major cause. The isotopic and fluid inclusion evidence suggests that magmatic fluids carrying the ore elements were mixed with metamorphic fluids. The emplacement of plutonic intrusions in shallow metasedimentary rocks generates convective systems (e.g., Jackson et al., 1982; Sheppard, 1977; Taylor, 1978). During the Logrosán granite emplacement, convective cells were produced in the adjacent SGC metasedimentary-rocks, not only in those affected by contact metamorphism. The convective cells may have allowed the circulation of volatile-rich fluids derived from the metasedimentary host rocks into the granite, as suggested for the Cornubian batholith by Wilkinson (1990). This would explain the prevalence of N_2–(CH_4) fluids over CO_2 during most of the fluid evolution of the Logrosán ore deposits and the metamorphic isotopic signatures. The magmatic fluids, enriched in F and B, concentrated towards the roof of the granite stock causing contact metasomatism (tourmalinization). At the same time, the overpressure caused an intense hydrofracturing, and the subsequently fluid mixing and release of pressure caused the cassiterite precipitation.

The P–T evolution of the ore deposition is based on estimated temperatures by isotope thermometry and arsenopyrite chemistry combined with those calculated from fluid inclusion isochores. In the case of the Oxide Stage, temperatures have been taken from the quartz–cassiterite geothermometry. The upper temperature limit taken for the Sulfide Stage corresponds to the arsenopyrite geothermometer; the lower limit coincides with the minimal homogenization temperature for Type-II fluid inclusion; a unique critical homogenization temperature found in Type-II fluid inclusions is also taken into account. The pressure limits have been estimated with the isochores. Thus, the P–T conditions of the Logrosán ore deposits are located approximately at 460–540 °C and 120–270 MPa for the Oxide Stage; and at 320–460 °C and 30–160 MPa for the Sulfide Stage (Fig. 11).

6. Conclusions

The fluids involved in the Logrosán ore deposits and the geochronological data allow interpreting a Sn–W ore formation model from the granite emplacement (at ca. 308 Ma) towards the ore precipitation (308–306 Ma and ~303 Ma). The granite emplacement into shallow levels, the metasomatism deduced by the host rock alteration, and the fluid inclusion and stable isotope evidence suggest that a relatively long-term interaction of the granite with the host-rocks occurred during the contact metamorphism. This implies that large hydrothermal convective systems involved fluid circulation through the nearby metasediments. The fluids derived from the metasedimentary organic-rich host rocks were enriched in volatiles, such as CH_4 and N_2. They may have circulated through the metasedimentary host rocks and the granite. The source of metals is inferred to be the highly fractionated Logrosán granite, enriched in tin and other incompatible elements. The magmatic fluids were probably concentrated to the roof of the cupola causing the contact metasomatism. An intense fracturing resulting from the overpressure in the granite cupola caused a release of pressure, an increase of the oxygen fugacity, and the mixing of metamorphic (organogenic) and magmatic fluids. Subsequently, the tin complexes were destabilized and the ores precipitated.

This is one of the few Sn–(W) granite-related ore deposits where the nature and sources of the fluids involved in the mineralization are strongly constrained by the composition of fluid inclusions and stable isotope signatures. The implication of non-magmatic fluids derived from the

metasedimentary country rocks on the cassiterite precipitation could contribute to the discussion on the origin of similar Sn–W ore deposits.

Acknowledgments

References

Alderton, D.H.M., Harmon, R.S., 1991. Fluid inclusion and stable isotope evidence for the origin of mineralizing fluids in south-west England. Mineral. Mag. 55, 605–611. http://dx.doi.org/10.1180/minmag.1991.055.381.13.

Antunes, I., Neiva, A., Silva, M., Corfu, F., 2008. Geochemistry of S-type granitic rocks from the reversely zoned Castelo Branco pluton (central Portugal). Lithos 103, 445–465. http://dx.doi.org/10.1016/j.lithos.2007.10.003.

Bakker, R.J., 2003. Package FLUIDS 1. Computer programs for analysis of fluid inclusion data and for modelling bulk fluid properties. Chem. Geol. 194, 3–23.

Bodnar, R., 1993. Revised equation and table for determining the freezing point depression of H_2O–NaCl solutions. Geochim. Cosmochim. Acta 57, 683–684. http://dx.doi.org/10.1016/0016-7037(93)90378-A.

Borthwick, J., Harmon, R.S., 1982. A note regarding ClF_3 as an alternative to BrF_5 for oxygen isotope analysis. Geochim. Cosmochim. Acta 46, 1665–1668.

Bottinga, Y., Javoy, M., 1975. Oxygen isotope partitioning among the minerals in igneous and metamorphic rocks. Rev. of Geophy. 13, 401–418. http://dx.doi.org/10.1029/RG013i002p00401.

Breiter, K., Förster, H.J., Seltmann, R., 1999. Variscan silicic magmatism and related tin–tungsten mineralization in the Erzgebirge-Slavkovský les metallogenic province. Mineral. Deposita 34, 505–521. http://dx.doi.org/10.1007/s001260050217.

Burnham, C.W., 1997. In: Barnes, H.L. (Ed.), Magmas and Hydrothermal FluidsGeochemistry of Hydrothermal Ore Deposits vol. 3. John Wiley and Sons, Inc., New York, pp. 63–123.

Burnham, C.W., Ohmoto, H., 1980. Late-stage processes of felsic magmatism. In: Ishihara, S., Takenouchi, S. (Eds.), Granitic Magmatism and Related Mineralization: Tokyo, Japan, pp. 1–11.

Cepedal, A., Fuertes-Fuente, M., Martín-Izard, A., García-Nieto, J., Boiron, M.C., 2013. An intrusion-related gold deposit (IRGD) in the NW of Spain, the Linares deposit: igneous rocks, veins and related alterations, ore features and fluids involved. J. Geochem. Explor. 124, 101–126. http://dx.doi.org/10.1016/j.gexplo.2012.08.010.

Chacko, T., Hu, X., Mayeda, T.K., Clayton, R.N., Goldsmith, J.R., 1996. Oxygen isotope fractionations in muscovite, phlogopite, and rutile. Geochim. Cosmochim. Acta 60, 2595–2608. http://dx.doi.org/10.1016/0016-7037(96)00112-3.

Cheilletz, A., Pelleter, E., Martin-Izard, A., Tornos, F., 2005. World skarn deposits: skarns of Western Europe. Economic Geology 100th Anniversary Volume, pp. 1–10.

Chen, X.C., Hu, R.Z., Bi, X.W., Li, H.M., Lan, J.B., Zhao, C.H., Zhu, J.J., 2014. Cassiterite LA-MC-ICP-MS U/Pb and muscovite $^{40}Ar/^{39}Ar$ dating of tin deposits in the Tengchong-Lianghe tin district, NW Yunnan, China. Mineral. Deposita 1–18 http://dx.doi.org/10.1007/s00126-014-0513-8.

Cheng, Y., Mao, J., Yang, Z., 2012. Geology and vein tin mineralization in the Dadoushan deposit, Gejiu district, SW China. Mineral. Deposita 47, 701–712. http://dx.doi.org/10.1007/s00126-012-0409-4.

Cheng, Y., Mao, J., Chang, Z., Pirajno, F., 2013. The origin of the world class tin-polymetallic deposits in the Gejiu district, SW China: constraints from metal zoning characteristics and ^{40}Ar–^{39}Ar geochronology. Ore Geol. Rev. 53, 50–62. http://dx.doi.org/10.1016/j.oregeorev.2012.12.008.

Chesley, J.T., Halliday, A.N., Snee, L.W., Mezger, K., Sheperd, T.J., Scrivener, R.C., 1993. Thermochronology of the Cornubian Batholith in southwest England: implications for pluton emplacement and protracted hydrothermal mineralisation. Geochim. Cosmochim. Acta 57, 1817–1835. http://dx.doi.org/10.1016/0016-7037(93)90115-D.

Chicharro, E., Villaseca, C., Valverde-Vaquero, P., Belousova, E., López-García, J.Á., 2014. Zircon U–Pb and Hf isotopic constraints on the genesis of a post-kinematic S-type Variscan tin granite: the Logrosán cupola (Central Iberian Zone). J. Iber. Geol. 40, 451–470. http://dx.doi.org/10.5209/rev_JIGE.2014.v40.n3.43928.

Chicharro, E., Martín-Crespo, T., Gómez-Ortiz, D., López-García, J.Á., Oyarzun, R., Villaseca, C., 2015. Geology and gravity modeling of the Logrosán Sn–(W) ore deposits (Central Iberian Zone, Spain). Ore Geol. Rev. 65, 294–307. http://dx.doi.org/10.1016/j.oregeorev.2014.10.005.

Clayton, R.N., Mayeda, T.K., 1963. The use of bromine pentafluoride in the extraction of oxygen from oxides and silicates for isotopic analysis. Geochim. Cosmochim. Acta 27, 43–52. http://dx.doi.org/10.1016/0016-7037(63)90071-1.

Clayton, R.N., O'Neil, J.R., Mayeda, T.K., 1972. Oxygen isotope exchange between quartz and water. J. Geophys. Res. 77, 3057–3067. http://dx.doi.org/10.1016/0016-7037(79)90099-1.

Craig, H., 1961. Isotopic variations in meteoric waters. Science 133, 1702–1703.

Darbyshire, D.P.F., Shepherd, T.J., 1985. Chronology of granite magmatism and associated mineralization, SW England. J. Geol. Soc. Lond. 142, 1159–1177. http://dx.doi.org/10.1144/gsjgs.142.6.1159.

Derré, C., 1982. Caractéristiques de la distribution des gisements à étain et tungstène dans l'Ouest de l'Europe. Mineral. Deposita 17, 55–77.

Dewaele, S., De Clercq, F., Hulsbosch, N., Piessens, K., Boyce, A., Burgess, R., Muchez, P., 2015. Genesis of the vein-type tungsten mineralization at Nyakabingo (Rwanda) in the Karagwe–Ankole belt, Central Africa. Mineral. Deposita 1-25. http://dx.doi.org/10.1007/s00126-015-0608-x.

Dias, G., Leterrier, J., Mendes, A., Simoes, P., Bertrand, J., 1998. U–Pb zircon and monazite geochronology of post-collisional Hercynian granitoids from the Central Iberian Zone (northern Portugal). Lithos 45, 49–369. http://dx.doi.org/10.1016/S0024-4937(98)00039-5.

Dias, G., Simões, P., Ferreira, N., Leterrier, J., 2002. Mantle and crustal sources in the genesis of late-Hercynian granitoids (NW Portugal): geochemical and Sr–Nd isotopic constraints. Gondwana Res. 5, 87–305. http://dx.doi.org/10.1016/S1342-937X(05)70724-3.

Dolníček, Z., René, M., Prochaska, W., Kovář, M., 2012. Fluid evolution of the Hub Stock, Horní Slavkov–Krásno Sn–W ore district, Bohemian Massif, Czech Republic. Mineral. Deposita 47, 821–833. http://dx.doi.org/10.1007/s00126-012-0400-0.

Duan, Z., Møller, N., Weare, J.H., 1992. An equation of state for the CH_4–CO_2–H_2O system: I. Pure systems from 0 to 1000 °C and 0 to 8000 bar. Geochim. Cosmochim. Acta 56, 2605–2617. http://dx.doi.org/10.1016/0016-7037(92)90347-L.

Duan, Z., Møller, N., Weare, J.H., 1996. A general equation of state for supercritical fluid mixtures and molecular dynamics simulation of mixture PVTX properties. Geochim. Cosmochim. Acta 60, 1209–1216.

Dubessy, J., Nguyen-Trung, C., Cathelineau, M., Cuney, M., Leroy, J., Poty, B., Ramboz, C., Charoy, B., Weisbrod, A., Weisbrod, A., 1987. Physical and chemical controls (fO2, T, pH) of the opposite behaviour of U and Sn–W as examplified by hydrothermal deposits in France and Great-Britain, and solubility data. Bull. Mineral. 110, 261–281.

Dubessy, J., Poty, B., Ramboz, C., 1989. Advances in COHNS fluid geochemistry based on micro-Raman spectrometric analysis of fluid inclusions. Eur. J. Mineral. 517-534.

Eugster, H.P., Wilson, G.A., 1985. Transport and deposition of ore-forming elements in hydrothermal systems associated with granites. High Heat Production (HHP) Granites, Hydrothermal Circulation and Ore Genesis. The Inst. Min. Metal., pp. 87–98.

Fallick, A., McConville, P., Boyce, A., Burgess, R., 1992. Laser microprobe stable isotope measurements on geological materials: some experimental considerations (with special reference to 34S in sulphides). Chem. Geol. (Isot. Geosci. Sect.) 101, 53–61.

Flowers, G.C., 1979. Correction of Holloway's (1977) adaptation of the modified Redlich–Kwong equation of state for calculation of the fugacities of molecular species in supercritical fluids of geologic interest. Contrib. Mineral. Petrol. 69, 315–318. http://dx.doi.org/10.1007/BF00372333.

Fu, B., Mernagh, T.P., Fairmaid, A.M., Phillips, D., Kendrick, M.A., 2014. CH_4–N_2 in the Maldon gold deposit, central Victoria, Australia. Ore Geol. Rev. 58, 225–237. http://dx.doi.org/10.1016/j.oregeorev.2013.11.006.

Fuertes-Fuente, M., Martin-Izard, A., Boiron, M.C., Viñuela, J.M., 2000. P–T path and fluid evolution in the Franqueira granitic pegmatite, central Galicia, northwestern Spain. Can. Mineral. 38, 1163–1175. http://dx.doi.org/10.2113/gscanmin.38.5.1163.

Giuliani, G., 1984. Les concentrations filoniennes à tungstène-étain du massif granitique des Zaër (Maroc Central): minéralisations et phases fluides associées. Mineral. Deposita 19, 193–201. http://dx.doi.org/10.1007/BF00199785.

Giuliani, G., Li, Y.D., Sheng, T.F., 1988. Fluid inclusion study of Xihuashan tungsten deposit in the southern Jiangxi province, China. Mineral. Deposita 23, 24–33. http://dx.doi.org/10.1007/BF00204224.

Godfrey, J.D., 1962. The deuterium content of hydrous minerals from the east-central sierra Nevada and Yosemite National Park. Geochim. Cosmochim. Acta 26, 1215–1245.

Guo, X.P., Qian, Y.Q., 1997. Hydrogen isotopic fractionation and hydrogen diffusion in the tourmaline-water system. Geochim. Cosmochim. Acta 16, 4679–4688. http://dx.doi.org/10.1016/S0016-7037(97)00252–4.

Halter, W.E., Williams-Jones, A.E., 1996. The role of greisinization in cassiterite precipitation at the East Kemptville tin deposit, Nova Scotia. Econ. Geol. 91, 368–385. http://dx.doi.org/10.2113/gsecongeo.91.2.368.

Hoefs, J., 2009. Stable Isotope Geochemistry. sixth ed. Springer-Verlag, Berlin.

Hoefs, J., Emmermann, R., 1983. The oxygen isotope composition of Hercynian granites and pre-Hercynian gneisses from the Schwarzwald, SW Germany. Contrib. Mineral. Petrol. 83 (3), 320–329. http://dx.doi.org/10.1007/BF00371200.

Holloway, J.R., 1977. Fugacity and Activity of Molecular Species in Supercritical Fluids. Springer, Netherlands.

Huff, T.A., Nabelek, P.I., 2007. Production of carbonic fluids ##during metamorphism of graphitic pelites in a collisional orogen—an assessment from fluid inclusions. Geochim. Cosmochim. Acta 71 (20), 4997–5015. http://dx.doi.org/10.1016/j.gca.2007.08.001.

Ishihara, S., 1977. The magnetite-series and ilmenite-series granitic rocks. Min. Geol. 27, 293–305.

Ishihara, S., Sasaki, A., 1989. Sulfur isotopic ratios of the magnetite-series and ilmenite-series granitoids of the Sierra Nevada batholith—a reconnaissance study. Geology 17, 788–791. http://dx.doi.org/10.1130/0091-7613(1989)017<0788:SIROTM>2.3.CO;2.

Jackson, N.J., Halliday, A.N., Sheppard, S.M.F., Mitchell, J.G., 1982. Hydrothermal activity in the St. Just mining district, Cornwall, England. In: Evans, M. (Ed.), Metallization Associated With Acid Magmatism Chichester. Wiley, pp. 137–179.

Jenkin, G.R.T., 1988. Stable Isotope Studies in the Caledonides of SW Connemara. University of Glasgow, Ireland.

Jiang, S.Y., 1998. Stable and radiogenic isotope studies of tourmaline: an overview. J. Geosci. 43, 75–90.

Kelley, S., Fallick, A., 1990. High precision spatially resolved analysis of ^{34}S in sulphides using a laser extraction technique. Geochim. Cosmochim. Acta 54, 883–888.

Kelly, W.C., Rye, R.O., 1979. Geologic, fluid inclusions and stable isotope studies of the tin–tungsten deposits of Panasqueira, Portugal. Econ. Geol. 74, 1721–1822. http://dx.doi.org/10.2113/gsecongeo.74.8.1721.

Kent, A.J.R., McDougall, I., 1995. ^{40}Ar–^{39}Ar and U–Pb age constraints on the timing of gold mineralization in the Kalgoorlie gold field, Western Australia. Econ. Geol. 90, 845–859. http://dx.doi.org/10.2113/gsecongeo.90.4.845.

Knight, C.L., Bodnar, R.J., 1989. Synthetic fluid inclusions. IX. Critical PVTX properties of NaCl–H$_2$O solutions. Geochim. Cosmochim. Acta 53, 3–8. http://dx.doi.org/10.1016/0016-7037(89)90267-6.

Kotzer, T.G., Kyser, T.K., King, R.W., Kerrich, R., 1993. An empirical oxygen- and hydrogen-isotope geothermometer for quartz–tourmaline and tourmaline–water. Geochim. Cosmochim. Acta 57, 3421–3426.

Kretschmar, U., Scott, S.D., 1976. Phase relations involving arsenopyrite in the system Fe–As–S and their application. Can. Mineral. 14, 364–386.

Lehmann, B., 1990. Metallogeny of tinLecture notes in earth sciences 32. Springer-Verlag (211 pp.).

Liao, S., Chen, S., Deng, X., Li, P., Zhao, J., Liao, R., 2014. Fluid inclusion characteristics and geological significance of the Xi'ao copper–tin polymetallic deposit in Gejiu, Yunnan Province. J. Asian Earth Sci. 79, 455–467.

Linnen, R.L., Williams-Jones, A.E., 1995. Genesis of a magmatic metamorphic hydrothermal system; the Sn–W polymetallic deposits at Pilok, Thailand. Econ. Geol. 90, 1148–1166. http://dx.doi.org/10.2113/gsecongeo.90.5.1148.

Mark, D.M., Barfod, D.N., Stuart, F.M., Imlach, J., 2009. The ARGUS multi-collector noble gas mass spectrometer: performance for ^{40}Ar/^{39}Ar geochronology. Geochem. Geophys. Geosyst. 1-13.

Martínez Catalán, J.R., Arenas, R., García, F.D., Pascual, F.J.R., Abati, J., Marquínez, J., 1996. Variscan exhumation of a subducted Paleozoic continental margin: the basal units of the Ordenes Complex, Galicia, NW Spain. Tectonics 15, 106–121. http://dx.doi.org/10.1029/95TC02617.

Martínez-Abad, I., Cepedal, A., Arias, D., Martín-Izard, A., 2015. The Vilalba gold district, a new discovery in the Variscan terranes of the NW of Spain: a geologic, fluid inclusion and stable isotope study. Ore Geol. Rev. 66, 344–365. http://dx.doi.org/10.1016/j.oregeorev.2014.10.021.

Mateus, A., Noronha, F., 2001. Late-Variscan uplift of the Iberian Terrane as a response to isostatic rebound; implications for the brittle–ductile transition, fluid circulation and metallogenesis. Mem. Mus. Lab. Mineral. Geol. Univ. Porto 7, 295–298.

Mateus, A., Noronha, F., 2010. Sistemas mineralizantes epigenéticos na Zona Centro-Ibérica; expressão da estruturação orogénica meso- a tardivarisca. In: Cotelo Neiva, J.M., Ribeiro, A., Mendes Victor, L., Noronha, F., Magalhães Ramalho, M. (Eds.), Ciências Geológicas: Ensino, Investigação e sua História. Vol. II, Geologia Aplicada. ISBN: 978-989-96669-1-7, pp. 47–61.

Moura, A., Dória, A., Neiva, A.M.R., Leal Gomes, C., Creaser, R.A., 2014. Metallogenesis at the Carris W–Mo–Sn deposit (Gerês, Portugal): constraints from fluid inclusions, mineral geochemistry, Re–Os and He–Ar isotopes. Ore Geol. Rev. 56, 73–93. http://dx.doi.org/10.1016/j.oregeorev.2013.08.001.

Neiva, A.M.R., 1984. Geochemistry of tin-bearing granitic rocks. Chem. Geol. 43, 241–256. http://dx.doi.org/10.1016/0009-2541(84)90052-4.

Nekrasov, I.J., Sorokin, V.I., Osadchii, E.G., 1979. Fe and Zn partitioning between stannite and sphalerite and its application in geothermometry. Phys. Chem. Earth 11, 739–742.

Noronha, F., Vindel Catena, E., López García, J.Á., Dória, A., García García, E., Boiron, M.C., Cathelineau, M., 1999. Fluids related to tungsten ore deposits in northern Portugal and Spanish central system: a comparative study. Rev. Soc. Geol. Esp. 12, 397–403.

Ohmoto, H., 1972. Systematics of sulfur and carbon isotopes in hydrothermal ore deposits. Econ. Geol. 67 (5), 551–578.

Ohmoto, H., 1986. Stable isotope geochemistry of ore deposits. Rev. Mineral. Geochem 16 (1), 491–559.

Ohmoto, H.Y., Rye, R.O., 1979. Isotopes of sulfur and carbon. En: Geochemistry of Hydrothermal Ore Deposits. J. Wiley and Sons, New York, pp. 509–567.

O'Neil, J.R., 1986. Theoretical and experimental aspects of isotopic fractionation. In: Valley, J.W., Taylor Jr., H.P., O'Neil, J.R. (Eds.), Stable Isotopes in High Temperature Geological Processes. Reviews in Mineralogy 16, pp. 1–16.

O'Neil, J.R., Taylor, H.P., 1967. The oxygen isotope and cation exchange chemistry of feldspars. Am. Mineral. 52, 1414–1437.

Ortega, L., Oyarzun, R., Gallego, M., 1996. The Mari Rosa late Hercynian Sb–Au deposit, western Spain. Mineral. Deposita 31, 172–187. http://dx.doi.org/10.1007/BF00204025.

Pirajno, F., 1992. Hydrothermal Mineral Deposits. Principles and Fundamental Concepts for the Exploration Geologist. Springer-Verlag, Berlin.

Pohl, W., Günther, M.A., 1991. The origin of Kibaran (late Mid-Proterozoic) tin, tungsten and gold quartz vein deposits in Central Africa: a fluid inclusions study. Mineral. Deposita 26, 51–59. http://dx.doi.org/10.1007/BF00202365.

Polyakov, V.B., Mineev, S.D., Clayton, R.N., Hu, G., Gurevich, V.M., Khramov, D.A., Gavrichev, K.S., Gorbunov, V.E., Golushina, L.N., 2005. Oxygen isotope fractionation factors involving cassiterite (SnO$_2$): I. Calculation of reduced partition function ratios from heat capacity and X-ray resonant studies. Geochim. Cosmochim. Acta 69, 1287–1300. http://dx.doi.org/10.1016/j.gca.2004.08.034.

Ramboz, C., Schnapper, D., Dubessy, J., 1985. The evolution of H$_2$O–CO$_2$–CH$_4$-bearing fluid in a wolframite vein: reconstruction from fluid inclusion studies. Geochim. Cosmochim. Acta 49, 205–219. http://dx.doi.org/10.1016/0016-7037(85)90205-4.

Renne, P.R., Balco, G., Ludwig, K.R., Mundil, R., Min, K., 2011. Response to the comment by W.H. Schwarz et al. on joint determination of K-40 decay constants and Ar-40*/K-40

for the Fish Canyon sanidine standard, and improved accuracy for Ar-40/Ar-39 geochronology by PR Renne, et al. (2010). Geochim. Cosmochim. Acta 75, 5097–5100. http://dx.doi.org/10.1016/j.gca.2011.06.021.

Ribeiro, A., 1990. Central-Iberian Zone: introduction. In: Dallmeyer, R.D., Martínez García, E. (Eds.), Pre-Mesozoic Geology of Iberia. Springer Verlag, Berlín, pp. 143–144.

Rodríguez Alonso, M.D., Díez Balda, M.A., Perejón, A., Pieren, A., Liñán, E., López Díaz, F., Moreno, F., Gámez Vintaned, J.A., González Lodeiro, F., Martínez Poyatos, D., Vegas, R., 2004. La secuencia litoestratigráfica del Neoproterozoico-Cámbrico Inferior. In: Vera, J.A. (Ed.), Geología de España. SGE-IGME, Madrid, pp. 78–81.

Roedder, E., 1984. Fluid InclusionsReviews in Mineralogy 12. Mineralogical Society of America, Michigan.

Roedder, E., Bodnar, R.J., 1980. Geologic pressure determinations from fluid inclusion studies. Annu. Rev. Earth Planet. Sci. 8, 263.

Rollinson, H.R., 1993. Using Geochemical Data: Evaluation, Presentation, Interpretation. Longman, Harlow.

Romer, R.L., Kroner, U., 2015. Sediment and weathering control on the distribution of Paleozoic magmatic tin–tungsten mineralization. Mineral. Deposita 50, 327–338. http://dx.doi.org/10.1007/s00126-014-0540-5.

Romer, R.L., Thomas, R., Stein, H.J., Rhede, D., 2007. Dating multiply overprinted Sn-mineralized granites—examples from the Erzgebirge, Germany. Mineral. Deposita 42, 337–359. http://dx.doi.org/10.1007/s00126-006-0114-2.

Sharp, Z.D., Essene, E.J., Kelly, W.C., 1985. A re-examination of the arsenopyrite geothermometer: pressure considerations and applications to natural assemblages. J. Miner. Assoc. Can. 23, 517–534.

Shepherd, T.J., Bottrell, S.H., Miller, M.F., 1991. Fluid inclusion volatiles as an exploration guide to black shale-hosted gold deposits, Dolgellau gold belt, North Wales, UK. J. Geochem. Explor. 42, 5–24. http://dx.doi.org/10.1016/0375-6742(91)90058-3.

Sheppard, S.M.F., 1977. The Cornubian batholith, SW England: D/H and ^{18}O/^{16}O studies of kaolinite and other alteration minerals. J. Geol. Soc. 133 (6), 573–591. http://dx.doi.org/10.1144/gsjgs.133.6.0573.

Sheppard, S.M., 1986. Characterization and isotopic variations in natural waters. Rev. Mineral. Geochem. 16 (1), 165–183.

Sheppard, S.M., Nielsen, R.L., Taylor, H.P., 1969. Oxygen and hydrogen isotope ratios of clay minerals from porphyry copper deposits. Econ. Geol. 64 (7), 755–777.

Sillitoe, R.H., 1994. Erosion and collapse of volcanoes: causes of telescoping in intrusion-centered ore deposits. Geology 22, 945–948. http://dx.doi.org/10.1130/0091-7613(1994)022<0945:EACOVC>2.3.CO;2.

Snee, L.W., Sutter, J.F., Kelly, W.C., 1988. Thermochronology of economic mineral deposits; dating the stages of mineralization at Panasqueira, Portugal, by high-precision ^{40}/^{39}Ar age spectrum techniques on muscovite. Econ. Geol. 83, 335–354. http://dx.doi.org/10.2113/gsecongeo.83.2.335.

Sparks, R.S.J., Folkes, C.B., Humphreys, M.C.S., Barfod, D.N., Clavero, J., Sunagua, M.C., McNutt, S., Pritchard, M.E., 2008. Uturuncu volcano, Bolivia: volcanic unrest due to mid-crustal magma intrusion. Am. J. Sci. 308, 727–769.

Suzuoki, T., Epstein, S., 1976. Hydrogen isotope fractionation between OH-bearing minerals and water. Geochim. Cosmochim. Acta 40, 1229–1240. http://dx.doi.org/10.1016/0016-7037(76)90158-7.

Tartèse, R., Boulvais, P., 2010. Differentiation of peraluminous leucogranites en route to the surface. Lithos 114 (3), 353–368. http://dx.doi.org/10.1016/j.lithos.2009.09.011.

Taylor, H.P., 1974. The application of oxygen and hydrogen isotope studies to problems of hydrothermal alteration and ore deposition. Econ. Geol. 69 (6), 843–883.

Taylor, H.P., 1978. Oxygen and hydrogen isotope studies of plutonic granitic rocks. Earth Planet. Sci. Lett. 38 (1), 177–210. http://dx.doi.org/10.1016/0012-821X(78)90131-0.

Thiéry, R., van den Kerkhof, A.M., Dubessy, J., 1994. vX properties of CH$_4$–CO2 and CO$_2$–N$_2$ fluid inclusions; modelling for T < 31 °C and P < 400 bars. Eur. J. Mineral. 6 (6), 753–771.

Van den Kerkhof, A., 1988. Phase transitions and molar volumes of CO$_2$–CH$_4$–N$_2$ inclusions. Bull. Mineral. 111 (3–4), 257–266.

Van den Kerkhof, A.M., 1990. Isochoric phase diagrams in the systems CO$_2$–CH$_4$ and CO$_2$–N$_2$: application to fluid inclusions application to fluid inclusions. Geochim. Cosmochim. Acta 54, 621–629. http://dx.doi.org/10.1016/0016-7037(90)90358-R.

Van den Kerkhof, A., Thiéry, R., 2001. Carbonic inclusions. Lithos 55, 49–68. http://dx.doi.org/10.1016/S0024-4937(00)00038-4.

Villaseca, C., Merino, E., Oyarzun, R., Orejana, D., Pérez-Soba, C., Chicharro, E., 2014. Contrasting chemical and isotopic signatures from Neoproterozoic metasedimentary rocks in the Central Iberian Zone (Spain) of pre-Variscan Europe: implications for terrane analysis and early Ordovician magmatic belts. Precambrian Res. 245, 131–145. http://dx.doi.org/10.1016/j.precamres.2014.02.006.

Vindel, E., López-García, J.Á., García, E., Boiron, M.C., Cathelineau, M., 1996. Estudio de inclusiones fluidas en granitos microfisurados. Mineralizaciones de W-Sn del Sistema Central Español. Geogaceta 20, 1558–1560.

Wagner, T., Boyce, A.J., Jonsson, E., Fallick, A.E., 2004. Laser microprobe sulphur isotope analysis of arsenopyrite: experimental calibration and application to the Boliden Au–Cu–As massive sulphide deposit. Ore Geol. Rev. 25, 311–325.

Watson, E.B., Harrison, T.M., 1983. Zircon saturation revisited: temperature and composition effects in a variety of crustal magma types. Earth Planet. Sci. Lett. 64, 295–304. http://dx.doi.org/10.1016/0012-821X(83)90211-X.

Wilkinson, J.J., 1990. The role of metamorphic fluids in the development of the Cornubian Orefield: fluid inclusion evidence from south Cornwall. Mineral. Mag. 54, 219–230. http://dx.doi.org/10.1180/minmag.1990.054.375.08.

Xu, G., 2000. Methane-rich fluid inclusions in the Proterozoic Zn–Pb–Ag deposit at Dugald River, NW Queensland: potential as an exploration guide. Appl. Geochem. 15, 1–12. http://dx.doi.org/10.1016/S0883-2927(99)00019-0.

Yuan, S., Peng, J., Hao, S., Li, H., Geng, J., Zhang, D., 2011. In situ LA-MC-ICP-MS and ID-TIMS U–Pb geochronology of cassiterite in the giant Furong tin deposit,

Hunan Province, South China: new constraints on the timing of tin–polymetallic mineralization. Ore Geol. Rev. 43, 235–242. http://dx.doi.org/10.1016/j.oregeorev.2011.08.002.

Yushan, L., Shuqing, C., 1986. An experimental study on cassiterite solubility and tin transport during mineralization. Acta Geol. Sin. 1, 78–88.

Zhang, D., Peng, J., Coulson, I.M., Hou, L., Li, S., 2014. Cassiterite U–Pb and muscovite ^{40}Ar–^{39}Ar age constraints on the timing of mineralization in the Xuebaoding Sn–W–Be deposit, western China. Ore Geol. Rev. 62, 315–322. http://dx.doi.org/10.1016/j.oregeorev.2014.04.011.

Zheng, Y.F., 1991. Calculation of oxygen isotope fractionation in metal oxides. Geochim. Cosmochim. Acta 55, 2299–2307. http://dx.doi.org/10.1016/0016-7037(91)90105-E.

Zheng, Y.F., 1993. Calculation of oxygen isotope fractionation in hydroxyl-bearing silicates. Earth Planet. Sci. Lett. 120, 247–263. http://dx.doi.org/10.1016/0012-821X(93)90243-3.